Search of S3 LIGO data for gravitational wave signals from spinning black hole and neutron star binary inspirals

B. Abbott,[14] R. Abbott,[14] R. Adhikari,[14] J. Agresti,[14] P. Ajith,[2] B. Allen,[2,51] R. Amin,[18] S. B. Anderson,[14] W. G. Anderson,[51] M. Arain,[39] M. Araya,[14] H. Armandula,[14] M. Ashley,[4] S. Aston,[38] P. Aufmuth,[36] C. Aulbert,[1] S. Babak,[1] S. Ballmer,[14] H. Bantilan,[8] B. C. Barish,[14] C. Barker,[15] D. Barker,[15] B. Barr,[40] P. Barriga,[50] M. A. Barton,[40] K. Bayer,[17] J. Betzwieser,[17] P. T. Beyersdorf,[27] B. Bhawal,[14] I. A. Bilenko,[21] G. Billingsley,[14] R. Biswas,[51] E. Black,[14] K. Blackburn,[14] L. Blackburn,[17] D. Blair,[50] B. Bland,[15] J. Bogenstahl,[40] L. Bogue,[16] R. Bork,[14] V. Boschi,[14] S. Bose,[52] P. R. Brady,[51] V. B. Braginsky,[21] J. E. Brau,[43] M. Brinkmann,[2] A. Brooks,[37] D. A. Brown,[14,6] A. Bullington,[30] A. Bunkowski,[2] A. Buonanno,[41] O. Burmeister,[2] D. Busby,[14] R. L. Byer,[30] L. Cadonati,[17] G. Cagnoli,[40] J. B. Camp,[22] J. Cannizzo,[22] K. Cannon,[51] C. A. Cantley,[40] J. Cao,[17] L. Cardenas,[14] G. Castaldi,[46] C. Cepeda,[14] E. Chalkley,[40] P. Charlton,[9] S. Chatterji,[14] S. Chelkowski,[2] Y. Chen,[1] F. Chiadini,[45] N. Christensen,[8] J. Clark,[40] P. Cochrane,[2] T. Cokelaer,[7] R. Coldwell,[39] R. Conte,[45] D. Cook,[15] T. Corbitt,[17] D. Coyne,[14] J. D. E. Creighton,[51] R. P. Croce,[46] D. R. M. Crooks,[40] A. M. Cruise,[38] A. Cumming,[40] J. Dalrymple,[31] E. D'Ambrosio,[14] K. Danzmann,[36,2] G. Davies,[7] D. DeBra,[30] J. Degallaix,[50] M. Degree,[30] T. Demma,[46] V. Dergachev,[42] S. Desai,[32] R. DeSalvo,[14] S. Dhurandhar,[13] M. Díaz,[33] J. Dickson,[4] A. Di Credico,[31] G. Diederichs,[36] A. Dietz,[7] E. E. Doomes,[29] R. W. P. Drever,[5] J.-C. Dumas,[50] R. J. Dupuis,[14] J. G. Dwyer,[10] P. Ehrens,[14] E. Espinoza,[14] T. Etzel,[14] M. Evans,[14] T. Evans,[16] S. Fairhurst,[7,14] Y. Fan,[50] D. Fazi,[14] M. M. Fejer,[30] L. S. Finn,[32] V. Fiumara,[45] N. Fotopoulos,[51] A. Franzen,[36] K. Y. Franzen,[39] A. Freise,[38] R. Frey,[43] T. Fricke,[44] P. Fritschel,[17] V. V. Frolov,[16] M. Fyffe,[16] V. Galdi,[46] J. Garofoli,[15] I. Gholami,[1] J. A. Giaime,[16,18] S. Giampanis,[44] K. D. Giardina,[16] K. Goda,[17] E. Goetz,[42] L. M. Goggin,[14] G. González,[18] S. Gossler,[4] A. Grant,[40] S. Gras,[50] C. Gray,[15] M. Gray,[4] J. Greenhalgh,[26] A. M. Gretarsson,[11] R. Grosso,[33] H. Grote,[2] S. Grunewald,[1] M. Guenther,[15] R. Gustafson,[42] B. Hage,[36] D. Hammer,[51] C. Hanna,[18] J. Hanson,[16] J. Harms,[2] G. Harry,[17] E. Harstad,[43] T. Hayler,[26] J. Heefner,[14] I. S. Heng,[40] A. Heptonstall,[40] M. Heurs,[2] M. Hewitson,[2] S. Hild,[36] E. Hirose,[31] D. Hoak,[16] D. Hosken,[37] J. Hough,[40] D. Hoyland,[38] S. H. Huttner,[40] D. Ingram,[15] E. Innerhofer,[17] M. Ito,[43] Y. Itoh,[51] A. Ivanov,[14] B. Johnson,[15] W. W. Johnson,[18] D. I. Jones,[47] G. Jones,[7] R. Jones,[40] L. Ju,[50] P. Kalmus,[10] V. Kalogera,[24] D. Kasprzyk,[38] E. Katsavounidis,[17] K. Kawabe,[15] S. Kawamura,[23] F. Kawazoe,[23] W. Kells,[14] D. G. Keppel,[14] F. Ya. Khalili,[21] C. Kim,[24] P. King,[14] J. S. Kissel,[18] S. Klimenko,[39] K. Kokeyama,[23] V. Kondrashov,[14] R. K. Kopparapu,[18] D. Kozak,[14] B. Krishnan,[1] P. Kwee,[36] P. K. Lam,[4] M. Landry,[15] B. Lantz,[30] A. Lazzarini,[14] M. Lei,[14] J. Leiner,[52] V. Leonhardt,[23] I. Leonor,[43] K. Libbrecht,[14] P. Lindquist,[14] N. A. Lockerbie,[48] M. Longo,[45] M. Lormand,[16] M. Lubinski,[15] H. Lück,[36,2] B. Machenschalk,[1] M. MacInnis,[17] M. Mageswaran,[14] K. Mailand,[14] M. Malec,[36] V. Mandic,[14] S. Marano,[45] S. Márka,[10] J. Markowitz,[17] E. Maros,[14] I. Martin,[40] J. N. Marx,[14] K. Mason,[17] L. Matone,[10] V. Matta,[45] N. Mavalvala,[17] R. McCarthy,[15] D. E. McClelland,[4] S. C. McGuire,[29] M. McHugh,[20] K. McKenzie,[4] S. McWilliams,[22] T. Meier,[36] A. Melissinos,[44] G. Mendell,[15] R. A. Mercer,[39] S. Meshkov,[14] E. Messaritaki,[14] C. J. Messenger,[40] D. Meyers,[14] E. Mikhailov,[17] S. Mitra,[13] V. P. Mitrofanov,[21] G. Mitselmakher,[39] R. Mittleman,[17] O. Miyakawa,[14] S. Mohanty,[33] G. Moreno,[15] K. Mossavi,[2] C. MowLowry,[4] A. Moylan,[4] D. Mudge,[37] G. Mueller,[39] S. Mukherjee,[33] H. Müller-Ebhardt,[2] J. Munch,[37] P. Murray,[40] E. Myers,[15] J. Myers,[15] T. Nash,[14] G. Newton,[40] A. Nishizawa,[23] K. Numata,[22] B. O'Reilly,[16] R. O'Shaughnessy,[24] D. J. Ottaway,[17] H. Overmier,[16] B. J. Owen,[32] Y. Pan,[41] M. A. Papa,[1,51] V. Parameshwaraiah,[15] P. Patel,[14] M. Pedraza,[14] S. Penn,[12] V. Pierro,[46] I. M. Pinto,[46] M. Pitkin,[40] H. Pletsch,[2] M. V. Plissi,[40] F. Postiglione,[45] R. Prix,[1] V. Quetschke,[39] F. Raab,[15] D. Rabeling,[4] H. Radkins,[15] R. Rahkola,[43] N. Rainer,[2] M. Rakhmanov,[32] M. Ramsunder,[32] S. Ray-Majumder,[51] V. Re,[38] H. Rehbein,[2] S. Reid,[40] D. H. Reitze,[39] L. Ribichini,[2] R. Riesen,[16] K. Riles,[42] B. Rivera,[15] N. A. Robertson,[14,40] C. Robinson,[7] E. L. Robinson,[38] S. Roddy,[16] A. Rodriguez,[18] A. M. Rogan,[52] J. Rollins,[10] J. D. Romano,[7] J. Romie,[16] R. Route,[30] S. Rowan,[40] A. Rüdiger,[2] L. Ruet,[17] P. Russell,[14] K. Ryan,[15] S. Sakata,[23] M. Samidi,[14] L. Sancho de la Jordana,[35] V. Sandberg,[15] V. Sannibale,[14] S. Saraf,[25] P. Sarin,[17] B. S. Sathyaprakash,[7] S. Sato,[23] P. R. Saulson,[31] R. Savage,[15] P. Savov,[6] S. Schediwy,[50] R. Schilling,[2] R. Schnabel,[2] R. Schofield,[43] B. F. Schutz,[1,7] P. Schwinberg,[15] S. M. Scott,[4] A. C. Searle,[4] B. Sears,[14] F. Seifert,[2] D. Sellers,[16] A. S. Sengupta,[7] P. Shawhan,[41] D. H. Shoemaker,[17] A. Sibley,[16] J. A. Sidles,[49] X. Siemens,[14,6] D. Sigg,[15] S. Sinha,[30] A. M. Sintes,[35,1] B. J. J. Slagmolen,[4] J. Slutsky,[18] J. R. Smith,[2] M. R. Smith,[14] K. Somiya,[2,1] K. A. Strain,[40] D. M. Strom,[43] A. Stuver,[32] T. Z. Summerscales,[3] K.-X. Sun,[30] M. Sung,[18] P. J. Sutton,[14] H. Takahashi,[1] D. B. Tanner,[39] R. Taylor,[14] R. Taylor,[40] J. Thacker,[16] K. A. Thorne,[32] K. S. Thorne,[6] A. Thüring,[36] K. V. Tokmakov,[40] C. Torres,[33] C. Torrie,[40] G. Traylor,[16] M. Trias,[35] W. Tyler,[14] D. Ugolini,[34] K. Urbanek,[30] H. Vahlbruch,[36] M. Vallisneri,[6] C. Van Den Broeck,[7] M. Varvella,[14] S. Vass,[14] A. Vecchio,[38] J. Veitch,[40] P. Veitch,[37] A. Villar,[14] C. Vorvick,[15] S. P. Vyachanin,[21] S. J. Waldman,[14] L. Wallace,[14] H. Ward,[40] R. Ward,[14] K. Watts,[16] A. Weidner,[2] M. Weinert,[2] A. Weinstein,[14] R. Weiss,[17] S. Wen,[18] K. Wette,[4] J. T. Whelan,[1] S. E. Whitcomb,[14] B. F. Whiting,[39] C. Wilkinson,[15] P. A. Willems,[14] L. Williams,[39] B. Willke,[36,2] I. Wilmut,[26] W. Winkler,[2] C. C. Wipf,[17] S. Wise,[39] A. G. Wiseman,[51] G. Woan,[40] D. Woods,[51] R. Wooley,[16] J. Worden,[15] W. Wu,[39] I. Yakushin,[16] H. Yamamoto,[14] Z. Yan,[50] S. Yoshida[28]

N. Yunes,[32] M. Zanolin,[17] J. Zhang,[42] L. Zhang,[14] C. Zhao,[50] N. Zotov,[19] M. Zucker,[17] H. zur Mühlen,[36] and J. Zweizig[14]

(The LIGO Scientific Collaboration, http://www.ligo.org)

[1]Albert-Einstein-Institut, Max-Planck-Institut für Gravitationsphysik, D-14476 Golm, Germany
[2]Albert-Einstein-Institut, Max-Planck-Institut für Gravitationsphysik, D-30167 Hannover, Germany
[3]Andrews University, Berrien Springs, MI 49104 USA
[4]Australian National University, Canberra, 0200, Australia
[5]California Institute of Technology, Pasadena, CA 91125, USA
[6]Caltech-CaRT, Pasadena, CA 91125, USA
[7]Cardiff University, Cardiff, CF24 3AA, United Kingdom
[8]Carleton College, Northfield, MN 55057, USA
[9]Charles Sturt University, Wagga Wagga, NSW 2678, Australia
[10]Columbia University, New York, NY 10027, USA
[11]Embry-Riddle Aeronautical University, Prescott, AZ 86301 USA
[12]Hobart and William Smith Colleges, Geneva, NY 14456, USA
[13]Inter-University Centre for Astronomy and Astrophysics, Pune - 411007, India
[14]LIGO - California Institute of Technology, Pasadena, CA 91125, USA
[15]LIGO Hanford Observatory, Richland, WA 99352, USA
[16]LIGO Livingston Observatory, Livingston, LA 70754, USA
[17]LIGO - Massachusetts Institute of Technology, Cambridge, MA 02139, USA
[18]Louisiana State University, Baton Rouge, LA 70803, USA
[19]Louisiana Tech University, Ruston, LA 71272, USA
[20]Loyola University, New Orleans, LA 70118, USA
[21]Moscow State University, Moscow, 119992, Russia
[22]NASA/Goddard Space Flight Center, Greenbelt, MD 20771, USA
[23]National Astronomical Observatory of Japan, Tokyo 181-8588, Japan
[24]Northwestern University, Evanston, IL 60208, USA
[25]Rochester Institute of Technology, Rochester, NY 14623, USA
[26]Rutherford Appleton Laboratory, Chilton, Didcot, Oxon OX11 0QX United Kingdom
[27]San Jose State University, San Jose, CA 95192, USA
[28]Southeastern Louisiana University, Hammond, LA 70402, USA
[29]Southern University and A&M College, Baton Rouge, LA 70813, USA
[30]Stanford University, Stanford, CA 94305, USA
[31]Syracuse University, Syracuse, NY 13244, USA
[32]The Pennsylvania State University, University Park, PA 16802, USA
[33]The University of Texas at Brownsville and Texas Southmost College, Brownsville, TX 78520, USA
[34]Trinity University, San Antonio, TX 78212, USA
[35]Universitat de les Illes Balears, E-07122 Palma de Mallorca, Spain
[36]Universität Hannover, D-30167 Hannover, Germany
[37]University of Adelaide, Adelaide, SA 5005, Australia
[38]University of Birmingham, Birmingham, B15 2TT, United Kingdom
[39]University of Florida, Gainesville, FL 32611, USA
[40]University of Glasgow, Glasgow, G12 8QQ, United Kingdom
[41]University of Maryland, College Park, MD 20742 USA
[42]University of Michigan, Ann Arbor, MI 48109, USA
[43]University of Oregon, Eugene, OR 97403, USA
[44]University of Rochester, Rochester, NY 14627, USA
[45]University of Salerno, 84084 Fisciano (Salerno), Italy
[46]University of Sannio at Benevento, I-82100 Benevento, Italy
[47]University of Southampton, Southampton, SO17 1BJ, United Kingdom
[48]University of Strathclyde, Glasgow, G1 1XQ, United Kingdom
[49]University of Washington, Seattle, WA, 98195
[50]University of Western Australia, Crawley, WA 6009, Australia
[51]University of Wisconsin-Milwaukee, Milwaukee, WI 53201, USA
[52]Washington State University, Pullman, WA 99164, USA

We report on the methods and results of the first dedicated search for gravitational waves emitted during the inspiral of compact binaries with spinning component bodies. We analyze 788 hours of data collected during the third science run (S3) of the LIGO detectors. We searched for binary systems using a detection template family designed specially to capture the effects of the spin-induced precession of the orbital plane. We present details of the techniques developed to enable this search for spin-modulated gravitational waves, highlighting the differences between this and other recent searches for binaries with non-spinning components. The template bank we employed was found to yield high matches with our spin-modulated target waveform for binaries with

masses in the asymmetric range $1.0\,M_\odot < m_1 < 3.0\,M_\odot$ and $12.0\,M_\odot < m_2 < 20.0\,M_\odot$ which is where we would expect the spin of the binary's components to have significant effect. We find that our search of S3 LIGO data had good sensitivity to binaries in the Milky Way and to a small fraction of binaries in M31 and M33 with masses in the range $1.0\,M_\odot < m_1, m_2 < 20.0\,M_\odot$. No gravitational wave signals were identified during this search. Assuming a binary population with spinning components and Gaussian distribution of masses representing a prototypical neutron star - black hole system with $m_1 \simeq 1.35 M_\odot$ and $m_2 \simeq 5 M_\odot$, we calculate the $90\%-$confidence upper limit on the rate of coalescence of these systems to be $15.9\,\mathrm{yr}^{-1}\mathrm{L}_{10}^{-1}$, where L_{10} is 10^{10} times the blue light luminosity of the Sun.

I. INTRODUCTION

Currently, there is a world-wide network of kilometer scale interferometric gravitational wave detectors that are either at or approaching their respective design sensitivities. The network includes the US Laser Interferometer Gravitational-wave Observatory (LIGO) [1, 2], the British-German GEO600 [3] and the French-Italian Virgo [4]. The radiation emitted during the inspiral stage of a stellar mass compact binary system is thought to be a likely candidate for the first direct detection of gravitational waves using these interferometers [5, 6]. The initial interferometers will be able to search for binary neutron star systems as far as the Virgo Cluster, and higher mass binaries which include black holes as far as the Coma supercluster. The range of merger rates consistent with present astrophysical understanding is summarized in Ref. [7]. When binary formation in star clusters is taken into account with relatively optimistic assumptions, detection rates could be as high as a few events per year for initial LIGO [8–10]. Merger rates derived for binary populations in galactic fields consistent with observational constraints from the known galactic neutron star - neutron star systems are highly uncertain but are likely to lie in the ranges (at 95% confidence) $0.1 - 15 \times 10^{-6}\mathrm{yr}^{-1}\,\mathrm{L}_{10}^{-1}$ and $0.15 - 10 \times 10^{-6}\mathrm{yr}^{-1}\,\mathrm{L}_{10}^{-1}$ for black hole - black hole and neutron star - black hole binaries respectively [11, 12]. The LIGO Scientific Collaboration (LSC) has searched for compact binaries with non-spinning stellar mass components in data collected during the first, second, third and fourth science runs (henceforth S1, S2, S3 and S4, respectively) [7, 13], by employing optimal matched filtering techniques [14] wherein detector data is cross-correlated with a bank of "templates" which represent the best current knowledge of the emitted waveforms.

Studies of compact binaries with spinning components [15–20] have revealed that general-relativistic dynamical coupling between the spin and orbital angular momenta (so long as they are not perfectly aligned or anti-aligned) will lead to precession of the binary's orbital plane which in turn causes a modulation of the observed gravitational waves' amplitude and phase. The binary's orbital angular momentum $\mathbf{L}$, and therefore its orbital plane, and the spin angular momenta of the binary's components $\mathbf{S}_1, \mathbf{S}_2$ will precess about its near constant total angular momentum $\mathbf{J} = \mathbf{L} + \mathbf{S}_1 + \mathbf{S}_2$. The gravitational waves observed from a binary depend upon the orientation of the binary relative to the detector and are strongest along the direction of its orbital angular momentum. The amplitude and phase of the gravitational waves emitted by the binary that will be observed at any particular (fixed) location will therefore be modulated by the precession of the binary's orbital plane. This precession of the orbital plane is nicely illustrated in Ref. [15] (see Fig. 2 and the appendix in particular). Figure 1 compares the gravitational waveforms we would expect to observe from two different binary systems, one consisting of non-spinning bodies and the other consisting of spinning bodies. The precession of the binary's orbital plane, which is related to the Lense–Thirring effect on gyroscopes in curved spacetimes [21], should not be confused with the in-plane precession of a binary's periastron which occurs in both spinning and non-spinning systems. In this search, we consider signals with frequencies of 70 Hz and above, corresponding to orbital frequencies of ≥ 35 Hz. We are thus sensitive only to the final stages of the binary inspiral. By this point, the binary orbit has been circularized due to the emission of gravitational waves (see Fig. 5 of Ref. [22]); so the precession of periastron degenerates into a secular term in the evolution of the phase.

The statistical distribution of the spins of black holes in inspiraling binaries is not well known [23, 24] and until recently the efforts have focused upon developing techniques for the detection of binary systems with non-spinning components (for recent reviews see Refs. [25, 26] and references therein). The presence of amplitude and phase modulations in the observed waveforms will reduce our detection efficiency when using matched filter templates which do not include spin effects [17–20]. These effects are small for low mass binaries or binaries with roughly equal component masses, but can be significant for high mass or asymmetric systems such as neutron star - black hole binaries.

This paper reports the methods and results of a search for gravitational waves emitted during the inspiral of binaries consisting of spinning compact objects. This search uses a detection template family designed to capture the spin-induced modulations of the gravitational waveform which could have resulted in them being missed by other searches targeted at non-spinning systems. This is the first time gravitational wave data has been searched for inspiral signals from binary systems with spinning component bodies.

LIGO consists of three detectors located at two sites across the US. The LIGO Hanford Observatory (LHO) in Washington state consists of two co-located interferometers of arm length 4km and 2km and are known as H1 and H2 respectively. The LIGO Livingston Observatory (LLO) in Louisiana consists of a single 4km interferometer known as L1. All three detectors were operated throughout S3 which spanned 70 days (1680 hours) between October 31, 2003 and January 9, 2004.
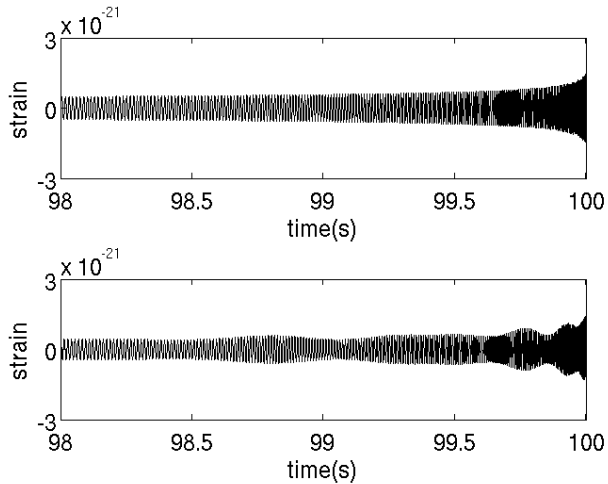
FIG. 1: The gravitational waveforms predicted from the late inspiral phase of two different neutron star - black hole systems, one consisting of non-spinning bodies (upper plot) and the other consisting of maximally spinning bodies (lower plot). Both systems are identical apart from the spin of their component bodies. Spin-induced precession of the binary's orbital plane causes modulation of the gravitational wave signal and can be clearly seen in the lower plot.

The gravitational waves emitted by stellar mass compact binaries are expected to be at frequencies detectable by LIGO during the final few seconds of the inspiral as well as the merger and ringdown stages of their evolution. We analyze S3 LIGO data using a detection template family [19] which efficiently captures the amplitude and phase modulations of the signal.

In Sec. II we discuss the evolution of spinning binary systems. In Sec. III we describe the waveforms that are used to model the emission of the target sources we are seeking to detect. These target waveforms include modulations to their amplitude and phase in order to simulate the effects of spin-induced precession of the source. In Sec. IV we describe the detection template family that we use to search for these target waveforms and in Sec. V we describe the design and testing of the template bank used. In Sec. VI we describe the S3 data set and summarize the data analysis pipeline. In Sec. VII we describe various vetoes which were identified as beneficial to this search. In Sec. VIII we detail results from this search. In the absence of a detection we will calculate an upper limit on the rate of coalescences using the measured efficiency of our search and an estimated population model of the distribution of binary systems in the Universe. In Sec. IX we perform an upper limit calculation based upon the loudest event candidate found in our search. Finally, in Sec. X we draw conclusions. Throughout we shall assume $G = c = 1$.

II. EVOLUTION OF SPINNING BINARY SYSTEMS

We briefly review the current literature regarding the formation and evolution of spinning binary systems. The literature available focuses mainly on neutron star - black hole (NS-BH) binaries (rather than BH-BH binaries). Later we shall show that the template bank used in this search is most sensitive to binaries with unequal masses such as NS-BH binaries. It is likely that the formation of BH-BH and NS-BH (and indeed NS-NS) systems are qualitatively similar and that the discussion here will be relevant to all cases.

A typical NS-BH evolution would involve two main sequence stars in binary orbit. As it evolves away from the main sequence, the more massive star would expand until it fills its Roche lobe before transferring mass to its companion. The more massive body would eventually undergo core-collapse to form a BH, and the system as a whole would become a high-mass X-ray binary. As the second body expands and evolves it would eventually fill its own Roche lobe and the binary would then go through a common-envelope phase. This common-envelope phase, characterized by unstable mass transfer, would be highly dissipative and would probably lead to both contraction and circularization of the binary's orbit. Accretion of mass can allow the BH to spin-up. It has been argued that the common-envelope phase, and associated orbital contraction, is essential in the formation of a binary which will coalesce within the Hubble time [23]. Finally the secondary body would undergo core-collapse to form a NS (or if massive enough, a BH). Prior to the supernova associated with the core-collapse of the secondary body we would expect the spin of the BH to be aligned with the binary's orbital angular momentum [23]. However, the "kick" associated with the supernova of the secondary body could cause the orbital angular momentum of the post-supernova binary to become tilted with respect to the orbital angular momentum of the pre-supernova binary. Since the BH would have a small cross-section with respect to the supernova kick we expect any change to the direction of its spin angular momentum to be negligible and that the BH spin would be misaligned with respect to the post-supernova orbital angular momentum [27]. The misalignment between the spin and orbital angular momentum is expected to be preserved until the system becomes detectable to ground based interferometers.

The magnitude of a compact object's spin is dependent upon both its spin at formation (i.e., birth-spin) and the spin it attains through subsequent accretion episodes. The dimensionless spin parameter χ is given by J/M^2 where J is the total angular momentum of the compact object and M is its mass. For a maximally spinning compact object we would have $\chi = 1$ and for a non-spinning object $\chi = 0$. Although the estimated birth-spins of NS and BHs are small, simulations have shown that accretion during a common-envelope phase can allow objects to achieve considerable or even near maximal spins [24]. Due to uncertainties in both the estimation of birth-spins and modelling of accretion induced spin-up predictions of binary's spin population are fairly uncertain. The upper bound on a BH's spin is expected to be $\chi \sim 0.998$. Torque caused by radiation emitted from the accretion disk getting swallowed by the BH counteracts the increase of spin caused as the BH accretes mass [28]. The upper bound of a NS's spin is estimated by calculating the spin which would cause it to break up using variety of models for its equation of

state. The upper limit is estimated to be $\chi \sim 0.7$ [29].

Techniques to measure the spin of accreting black holes using electromagnetic observations of their accretion disk are described in Ref. [30]. Using these techniques the spins of a black holes in a handful of X-ray binaries have been measured, in the case of GRS 1915+105 the black hole's spin was found to be $\chi > 0.98$ [31]. Recent observations of spin precession through measurement of pulse shapes from binary radio pulsars demonstrate misalignment between the orbital and spin angular momenta of these systems, see for example Ref. [32].

For optimal detection of gravitational waves using matched-filter techniques we must construct templates that represent our best predictions of the signal. These templates must model the spin-induced modulations to the waveform's amplitude and phase as accurately as possible while still resulting in a computationally manageable number of templates covering the detectable parameter space. It has been shown previously [17–20] that if spin effects are neglected when constructing our templates that our detection efficiency will decrease and some spinning binary systems will be missed. Spin effects are more pronounced when the system's spin angular momentum is larger than its orbital angular momentum. The Newtonian expression for the magnitude of the orbital angular momentum of a binary system is $|L_N| = \eta M^{5/3}\omega^{-1/3}$ where $M = m_1 + m_2$ is the total mass of the system, $\eta = m_1 m_2 / M^2$ is its symmetric mass ratio and ω is the instantaneous orbital frequency of the system. For given values of M and ω, the orbital angular momentum will be largest for binary systems with equal masses, $m_1 = m_2$. For systems with unequal masses such as NS-BH binaries, the orbital angular momentum will be smaller and the spin angular momentum will play a more significant role in the system's evolution. It will therefore be more susceptible to the effects of spin than equal mass systems (see Fig. 3 of Ref. [16]). For schemes that fail to take into account spin effects, detection efficiency will be worse for binaries with i) unequal mass components, ii) components with large spin magnitude and iii) when there is significant misalignment between the spins and the orbital angular momentum.

III. TARGET WAVEFORMS

In this section we describe the fiducial *target waveforms* used to represent the gravitational wave signals expected from binary systems of spinning compact objects. We adopt the post-Newtonian (PN) equations given out in Ref. [19] and based upon Refs. [15, 16, 33–38] (see Ref. [19] for a complete list of references to all original derivations), which model the inspiral of the binary in the adiabatic limit. In this limit the binary's components follow a sequence of shrinking instantaneously-circular orbits in a precessing orbital plane.

The instantaneous orbital frequency ω evolves according to Eq. (1) of Ref. [19], which has the structure

$$\frac{\dot{\omega}(t)}{\omega(t)^2} = F_{\dot{\omega}}\big(\omega(t), \hat{\mathbf{L}}_N(t)\cdot\hat{\mathbf{S}}_{1,2}(t), \hat{\mathbf{S}}_1(t)\cdot\hat{\mathbf{S}}_2(t); M, \eta, \chi_{1,2}\big),$$

(1)

with the total mass of the system M, the symmetric mass ratio η, the magnitudes of the binary's dimensionless spin parameters $\chi_{1,2}$, the direction of the Newtonian angular momentum $\hat{\mathbf{L}}_N(t)$ ($\propto \mathbf{r} \times \mathbf{v}$, perpendicular to the bodies velocity and the vector joining them), and the directions of the two spins $\hat{\mathbf{S}}_{1,2}(t)$. Orbital PN effects are included up to 3.5PN order, while spin effects are included up to 2PN order.

The two spins and the orbital angular momentum evolve according to standard general-relativistic precession equations, which are truncated consistently at the relevant PN order, and which have the structure

$$\dot{\hat{\mathbf{S}}}_1 = \mathbf{F}_{\dot{\hat{\mathbf{S}}}_1}\big(\omega, \hat{\mathbf{L}}_N, \hat{\mathbf{S}}_2; M, \eta, \chi_2\big) \times \hat{\mathbf{S}}_1,$$

$$\dot{\hat{\mathbf{S}}}_2 = \mathbf{F}_{\dot{\hat{\mathbf{S}}}_2}\big(\omega, \hat{\mathbf{L}}_N, \hat{\mathbf{S}}_1; M, \eta, \chi_1\big) \times \hat{\mathbf{S}}_2,$$

(2)

$$\dot{\hat{\mathbf{L}}}_N = \mathbf{F}_{\dot{\hat{\mathbf{L}}}_N}\big(\omega, \hat{\mathbf{L}}_N\cdot\hat{\mathbf{S}}_1, \hat{\mathbf{L}}_N\cdot\hat{\mathbf{S}}_2, \hat{\mathbf{S}}_1, \hat{\mathbf{S}}_2; M, \eta, \chi_1, \chi_2\big) \times \hat{\mathbf{L}}_N$$

(see Eqs. (2), (3), and (9) of Ref. [19]).

The gravitational strain perturbation h^{ij} is computed from the leading-order mass-quadrupole term specialized to circular orbits, following Finn and Chernoff [39] (see also Sec. II C of Ref. [19]). Since Finn and Chernoff use a fixed source coordinate system, the twice-differentiated mass-quadrupole tensor Q_c^{ij} is a function of the orbital phase $\int \omega\, dt$ and of $\hat{\mathbf{L}}_N(t)$. The response of a ground-based interferometric detector is obtained by projecting Q_c^{ij} onto a combination of unit vectors along the interferometer arms, which introduces a dependence on five angles that describe the relative direction (Θ and φ, which subsumes the initial orbital phase of the binary) and orientation (θ, ϕ, and ψ) between the detector and the Finn–Chernoff source frame.

Equations (1) and (2) are integrated numerically in the time domain until the minimum of the PN orbital energy $E_{3PN}(\omega, \hat{\mathbf{L}}_N, \hat{\mathbf{S}}_1, \hat{\mathbf{S}}_2, M, \eta, \chi_1, \chi_2)$ (see Eqs. (11) and (12) of Ref. [19]) is reached or until $\dot{\omega}$ becomes negative. No attempt is made to describe the waveform beyond this stopping point, where it is assumed that the adiabatic approximation must break down. Altogether, the waveforms are functions of four mass and spin constants (M, η, χ_1, and χ_2), of six angles describing the orientations of $\hat{\mathbf{L}}_N$, $\hat{\mathbf{S}}_1$, and $\hat{\mathbf{S}}_2$ at a fiducial time and frequency, the five direction and orientation angles and the distance of the detector from the source. We note that the angles Θ and φ are degenerate with the angles given implicitly when we define $\hat{\mathbf{L}}_N$. In this analysis we assume that the binary's orbits have become circularized (see brief discussion in Sec. II) and that the orbital eccentricity is zero. Given this assumption we are able to describe the binary using 15 independent parameters.

IV. DETECTION TEMPLATE FAMILY

As discussed in Sec. II, when the binary components carry significant spins which are not aligned with the orbital angular momentum, spin-orbit and spin-spin couplings can induce a strong precession of the orbital plane, thus causing substantial modulation of the gravitational waves' amplitude and phase

(see Fig. 1). Detection-efficient search templates must account for these effects of spin. A straightforward parametrization of search templates by the physical parameters that affect precession results in very large template banks, which is computationally prohibitive. It is then necessary to reduce the number of waveform parameters while still efficiently covering the parameter space of target waveforms.

We shall denote by "detection template family" (DTF) a family of signals that captures the essential features of the true waveforms, but depend on a smaller number of parameters, either physical or phenomenological. At their best, DTFs can reduce computational requirements while achieving essentially the same detection performance as true templates. However, DTFs can include non-physical signal shapes that may increase the number of noise-induced triggers, affecting the upper-limit studies. Moreover, DTFs are also less adequate for parameter estimation, because the mapping between template and binary parameters is not one-to-one.

In recent years several DTFs for precessing compact binaries have been proposed [15, 17–20, 27, 40, 41]. A DTF based on the so-called *Apostolatos ansatz* [15, 17] for the evolution of precession frequency was thoroughly investigated in Refs. [20, 40]. It was found that the computational requirements of the Apostolatos-type families are very high, and its signal-matching performances are not very satisfactory. An improved version using *spiky* templates was then proposed in Ref. [27].

After analyzing the physics of spinning-binary precession and waveform generation, the authors of Ref. [19] showed that the modulational effects can be isolated in the evolution of the two gravitational wave polarizations (i.e., h_+ and $h_\times$), which combined with the detector's antenna patterns yield its response. As a result, the detector's response can be written as the product of a carrier signal and a complex modulation factor, which can be handled using an extension of the Apostolatos ansatz. More explicitly, the modulated DTF in the frequency domain proposed in Ref. [19] reads:

$$h(\psi_{\mathrm{NM}}, t_0, \alpha_j; f) = \left[\sum_{j=1}^{3} (\alpha_j + i\alpha_{j+3}) h_j(f) \right] \times$$
$$e^{2\pi i f t_0} \theta(f_{\mathrm{cut}} - f) \quad (\text{for } f > 0) \tag{3}$$

with $h(f) = h^*(-f)$ for $f < 0$. The coefficients α_j in Eq. (3) are six real coefficients encoding the global phase, the strength of the amplitude modulation, its relative phase with respect to the leading order amplitude, and the internal (complex) phase of the modulations. The coefficient t_0 is the time of arrival and $\theta(...)$ is the Heaviside step function which is zero for all frequencies $f > f_{\mathrm{cut}}$. We use the parameter f_{cut} to terminate the template waveform once we believe it is no longer an accurate representation of the true gravitational waveform (generally due to deviation away from the adiabatic approximation).

In Eq. (3) the functions $h_j(f) = \mathcal{A}_j(f) e^{i\psi_{\mathrm{NM}}(f)}$ are the

basis-templates where $\mathcal{A}_j(f)$ are the real amplitude functions:

$$\mathcal{A}_1(f) = f^{-7/6}, \tag{4}$$
$$\mathcal{A}_2(f) = f^{-7/6} \cos(\mathcal{B}), \tag{5}$$
$$\mathcal{A}_3(f) = f^{-7/6} \sin(\mathcal{B}), \tag{6}$$

where $\mathcal{B} = \beta f^{-2/3}$ and β is related to the frequency of precession [41] and is used to capture the spin-induced modulation of the waveform. The function $\psi_{\mathrm{NM}}(f)$ represents the phase of the non-modulated carrier signal; it depends on the masses and spins of the binary's components and it can be computed in post-Newtonian (PN) theory. Here, as in Ref. [19], we express ψ_{NM} in terms of *only* two phenomenological parameters ψ_0 and ψ_3 [60], i.e.,

$$\psi_{\mathrm{NM}}(f) = f^{-5/3} (\psi_0 + \psi_3 f). \tag{7}$$

In the case of single-spin binaries (i.e., only one of the bodies has spin), it is possible to (analytically) relate the three phenomenological parameters ψ_0, ψ_3 and β with the four physical parameters M, η, κ_1 and χ_1 [41]. The physical parameter κ is the cosine of the angle between the direction of the (total) spin and the orbital angular momentum and in this case would be $\kappa_1 \equiv \hat{\mathbf{L}}_N \cdot \hat{\mathbf{S}}_1$. However, for double-spin binaries — which is the case investigated in this paper — the mapping is not analytical and the number of physical parameters is greater than four, resulting in an intractably large template bank. Within the spirit of DTF and, as a first step in implementing search templates for spinning, precessing binaries, we proceed here with the three phenomenological parameters ψ_0, ψ_3 and β.

The DTF described by Eq. (3) generalizes the Apostolatos ansatz in two ways: it allows a *complex* phase offset between i) the leading order $f^{-7/6}$ amplitude term (Eq. 4) and the sinusoidal amplitude terms (Eqs. 5 and 6) and ii) between the cosine and sine modulation terms. Quite interestingly, as shown in Ref. [41], by an appropriate choice of the phenomenological coefficients $\alpha_{1...6}$, the DTF also has the ability to generate higher harmonics which arise in the target signal discussed in Sec. III. Those higher harmonics are caused by oscillations in the components of the gravitational wave polarization tensor and not directly by the precession of the orbital angular momentum and spins, and should be reproduced by the search templates in order not to lose efficiency.

Henceforth, we will treat ψ_0, ψ_3 and β as *intrinsic* parameters and the $\alpha_{1...6}$ and t_0 as *extrinsic* parameters. Intrinsic parameters describe the source itself (e.g., masses, spins). To maximize the SNR with respect to the intrinsic parameters we must construct templates corresponding to different values of the intrinsic parameters and measure the SNR obtained by each of these templates with our detector data. On the other hand, extrinsic parameters describe the observer's relation to the source (e.g., distance of the source from the observer, the amplitude and time of arrival of the gravitational wave at the observer). Maximization of the SNR with respect to extrinsic parameters can be performed automatically (e.g., measurement of a signal's time of arrival using an FFT) and is computationally cheaper than maximization of the SNR with respect to the intrinsic parameters.

In practice we set f_{cut} to the frequency of the gravitational wave emission at the last stable orbit (LSO) which we estimate using

$$f_{\text{cut}} \approx f_{\text{LSO}} = \frac{M^{1/2}}{\pi r_{\text{LSO}}^{3/2}} \qquad (8)$$

where $r_{\text{LSO}} = 6M$ is the separation of the binary's components and the total mass M is estimated from ψ_0 and ψ_3 using approximate relationships between phenomenological and physical parameters we introduce in the next section, see Eqs. (13,14).

To assess whether a stretch of detector data contains a gravitational wave signal we calculate the signal-to-noise ratio (SNR) which is the cross-correlation of our templates with the data. The full process of deciding whether a detection has been made is described in Sec. VI of this paper and more fully in the companion papers [7, 26]. We can simplify the calculation of SNR by orthonormalization of the amplitude functions $\mathcal{A}_k$. We obtain the orthonormalized amplitude functions, denoted $\widehat{\mathcal{A}}_k$, using the Gram-Schmidt procedure which leads to the transformations:

$$\mathcal{A}_1 \rightarrow \widehat{\mathcal{A}}_1 = \frac{\mathcal{A}_1}{||\mathcal{A}_1||^{1/2}}$$

$$\mathcal{A}_2 \rightarrow \widehat{\mathcal{A}}_2 = \frac{\mathcal{A}_2 - \left\langle \mathcal{A}_2, \widehat{\mathcal{A}}_1 \right\rangle \widehat{\mathcal{A}}_1}{||\mathcal{A}_2 - \left\langle \mathcal{A}_2, \widehat{\mathcal{A}}_1 \right\rangle \widehat{\mathcal{A}}_1||^{1/2}} \qquad (9)$$

$$\mathcal{A}_3 \rightarrow \widehat{\mathcal{A}}_3 = \frac{\mathcal{A}_3 - \left\langle \mathcal{A}_3, \widehat{\mathcal{A}}_1 \right\rangle \widehat{\mathcal{A}}_1 - \left\langle \mathcal{A}_3, \widehat{\mathcal{A}}_2 \right\rangle \widehat{\mathcal{A}}_2}{||\mathcal{A}_3 - \left\langle \mathcal{A}_3, \widehat{\mathcal{A}}_1 \right\rangle \widehat{\mathcal{A}}_1 - \left\langle \mathcal{A}_3, \widehat{\mathcal{A}}_2 \right\rangle \widehat{\mathcal{A}}_2||}$$

where we use $||a||$ to represent the inner product of a function with itself: $||a|| = \langle a, a \rangle$. Throughout we will use the real-valued inner product:

$$\langle a, b \rangle = 4\Re \int_0^\infty df \frac{\tilde{a}^*(f)\tilde{b}(f)}{S_h(f)} \qquad (10)$$

where $S_h(f)$ is an estimate of the noise power spectral density of the data. The final form of the orthonormalized amplitude functions are very long and for that reason not reproduced here. The DTF in terms of the orthonormalized amplitude functions has the exact same form as that shown in Eq. (3) with h, h_j and α_j replaced by $\hat{h}$, $\hat{h}_j$ and $\hat{\alpha}_j$ respectively. Demanding templates normalized so that $\langle h, h \rangle = \left\langle \hat{h}, \hat{h} \right\rangle = 1$ leads to the constraint $\sum_{j=1}^{6} \hat{\alpha}_j^2 = 1$. Having defined the orthonormalized amplitude functions $\widehat{\mathcal{A}}_k$ we can calculate the SNR, ρ:

$$\rho = \max_{t_0,\alpha_j} \langle x, h(t_0, \alpha_j) \rangle = \max_{t_0} \sqrt{\sum_{j=1}^{6} \left\langle x, \hat{h}_j(t_0) \right\rangle^2}, \quad (11)$$

where x is the detector data and the orthonormalized basis-templates are given by

$$\begin{aligned}\hat{h}_j &= \widehat{\mathcal{A}}_j(f)e^{i\psi_{\text{NM}}(f)} \quad \text{for } j = 1, 2, 3 \text{ and} \\ \hat{h}_j &= i\widehat{\mathcal{A}}_{j-3}(f)e^{i\psi_{\text{NM}}(f)} \quad \text{for } j = 4, 5, 6. \quad (12)\end{aligned}$$

Note that we do not explicitly need to calculate $\alpha_{1\ldots6}$ in order to calculate the SNR but that they can be found simply if required: $\hat{\alpha}_j = \left\langle x, \hat{h}_j(t_0) \right\rangle / \rho$.

For Gaussian white noise, ρ^2 will, in general, have a χ^2 distribution with 6 degrees of freedom. In the case where the spin parameter $\beta = 0$ we find that $\widehat{\mathcal{A}}_2$ and $\widehat{\mathcal{A}}_3$ both vanish and that ρ^2 is described by a χ^2 distribution with 2 degrees of freedom. To reflect the increased freedom we choose a higher SNR threshold, $\rho_* = 12$ when $\beta \neq 0$ and a lower value of $\rho_* \approx 11.2$ when $\beta = 0$. These values were chosen to give approximately the same number of triggers when analyzing Gaussian white noise and to ensure that the number of triggers produced during the real search was manageable.

V. TEMPLATE BANK

Since we will not know the parameters describing an incident gravitational waveform a priori, we must filter our detector data with a set of templates known as a *template bank*. Neglecting the effects of noise, we would expect that the template yielding the largest SNR to be the best representation of an incoming signal. Due to the discrete nature of the template bank (it must be discrete since it can only contain a finite number of templates) we will lose SNR due to mismatches between the intrinsic parameters of any gravitational wave signal and the best template. By placing templates with an appropriate density, we can limit the maximum mismatch between signal and template intrinsic parameters and hence limit the loss of SNR caused by the discreteness of the bank. The spacing of templates in the intrinsic parameter space required to limit this mismatch can be found using the metric on the signal manifold [42, 43]. In this section we describe the calculation of the metric, the template placement algorithm and comparisons with other banks before discussing the testing of the bank using software-injected simulated signals.

A. Metric calculation

In this search we use a simple metric based on the strong modulation approximation described below. The rationale is that systems with waveforms only weakly modulated by spin-induced precession should be detectable with high efficiency by a non-spinning binary search, e.g., [7]. Thus we concentrate on designing a bank that will capture systems whose waveforms will be strongly modulated. The metric calculation and template placement (or tiling) algorithms become much simpler in the strong modulation limit. More recently, more precise treatments of the full metric on the DTF parameter space have become available [41, 44] and work is in progress to incorporate them into future searches.

In the strong modulation approximation, the orbital plane is assumed to precess many times as the gravitational wave sweeps through the LIGO band of good sensitivity. Also the opening angle between the orbital and spin angular momentum is assumed to be large, corresponding to large ampli-

tude modulations of the signal. Mathematically this corresponds to the statement that the precession phase $\mathcal{B}$ sweeps through many times 2π and thus that the basis-templates h_j are nearly orthonormal (without need for the Gram-Schmidt procedure). Below we shall see that this assumption places a condition on the precession parameter β, which for the initial LIGO design noise power spectral density [45] corresponds to $\beta \gtrsim 200\ \mathrm{Hz}^{2/3}$.

We can relate this condition for validity of the strong modulation approximation to the astrophysical parameters of system. Naïvely we can put the phenomenological parameters in terms of astrophysical parameters using:

$$\psi_0 = \frac{3}{128}[\pi(m_1+m_2)]^{-5/3}\frac{(m_1+m_2)^2}{m_1 m_2}, \qquad (13)$$

$$\psi_3 = -\frac{3\pi}{8}[\pi(m_1+m_2)]^{-2/3}\frac{(m_1+m_2)^2}{m_1 m_2}, \qquad (14)$$

$$\beta = 258\ \mathrm{Hz}^{2/3}\left(1+\frac{3m_2}{4m_1}\right)\frac{m_1}{m_2}\chi\left(\frac{M_\odot}{m_1+m_2}\right)^{2/3} (15)$$

acknowledging that, in reality, the true signal manifold and phenomenological template manifold do not map this simply. The equations for ψ_0 and ψ_3 can be found by considering the expansion for the gravitational wave phase $\psi(f)$ given in terms of masses (e.g., Eqs. (3.3) and (3.4) of [46]) and equating the dominant terms of this expansion to those with the same frequency exponent in the expansion for gravitational wave phase given in terms of $\psi_{0,1,\ldots}$ in [19, 47]. The effects of spin are neglected in these approximations of ψ_0 and ψ_3. The equation for β arises by recognizing that β is related to the evolution of the rate of precession, see Eq. (45) of [15] and [41] for further discussion [61].

The constraint for validity of the strong modulation approximation is that the mass ratio must satisfy $m_2/m_1 \gtrsim 2$. Also, we specify that the total mass be less than some value (here $\sim 15\ M_\odot$) so that the waveforms do not begin far enough into the non-linear region to require extra phenomenological parameters. Thus the parameter space region of such a search may be expressed solely in terms of the range of masses for the lower-mass body. In this search the range used for m_1 was $1.0\ M_\odot < m_1 < 3.0\ M_\odot$, a likely range of masses for neutron stars, and $6.0\ M_\odot < m_2 < 12.0\ M_\odot$ was used as the range for the more massive body. Thus, astrophysically this search is directed at NS-BH systems or BH-BH systems with unequal masses. These mass ranges are converted into ranges of ψ_0 and ψ_3 using Eqs. (13) and (14) which define the region of parameter space we populate with templates. Due to the inexact nature of these equations we know that the range of masses for which the template bank obtains its highest matches may differ from the range of masses we use to specify the region of (ψ_0, ψ_3). We will show in Sec. V C that a template bank generated using the range of masses just specified yields high matches (greater than 0.9) for binaries with physical masses in the asymmetric range $1.0\ M_\odot < m_1 < 3.0\ M_\odot$ and $12.0\ M_\odot < m_2 < 20.0\ M_\odot$. We shall also show that this search is efficient for non-spinning systems as well as for spinning ones.

We derive the metric components in the manner of

Ref. [42]. Starting from the detection statistic ρ^2 (the square of Eq. (11)), let us take our data x to have the form of a template with parameters slightly perturbed from those of the template h we filter it with:

$$\begin{aligned}
\tilde{x}(f) &= (\alpha_1 + i\alpha_2)e^{i(\psi_{\mathrm{NM}}+d\psi_{\mathrm{NM}})} \\
&+ (\alpha_3 + i\alpha_4)\cos(\mathcal{B}+d\mathcal{B})e^{i(\psi_{\mathrm{NM}}+d\psi_{\mathrm{NM}})} \\
&+ (\alpha_5 + i\alpha_6)\sin(\mathcal{B}+d\mathcal{B})e^{i(\psi_{\mathrm{NM}}+d\psi_{\mathrm{NM}})} \quad (16)
\end{aligned}$$

Note that only the intrinsic parameters are perturbed, as the maximization takes care of the extrinsic parameters. Expanding to second order in the perturbation, we have

$$\begin{aligned}
\tilde{x}(f) &\approx \left(1 + i\,d\psi_{\mathrm{NM}} - \frac{1}{2}d\psi_{\mathrm{NM}}^2\right)\Bigg\{(\alpha_1 + i\alpha_2)h_1 \\
&+ (\alpha_3 + i\alpha_4)\left[\left(1-\frac{1}{2}d\mathcal{B}^2\right)h_2 - d\mathcal{B}h_3\right] \\
&+ (\alpha_5 + i\alpha_6)\left[\left(1-\frac{1}{2}d\mathcal{B}^2\right)h_3 + d\mathcal{B}h_2\right]\Bigg\} (17)
\end{aligned}$$

Under the approximation that the h_j are orthonormal, we get

$$\begin{aligned}
\langle x, h_1\rangle &= \alpha_1\left[1-\frac{1}{2}F\left(d\psi_{\mathrm{NM}}^2\right)\right] - \alpha_2 F(d\psi_{\mathrm{NM}}), \\
\langle x, h_4\rangle &= \alpha_2\left[1-\frac{1}{2}F\left(d\psi_{\mathrm{NM}}^2\right)\right] + \alpha_1 F(d\psi_{\mathrm{NM}}), \\
\langle x, h_2\rangle &= \alpha_3\left[1-\frac{1}{2}F\left(d\psi_{\mathrm{NM}}^2\right) - \frac{1}{2}F\left(d\mathcal{B}^2\right)\right] \\
&\quad -\alpha_4 F(d\psi_{\mathrm{NM}}) + \alpha_5 F(d\mathcal{B}) - \alpha_6 F(d\psi_{\mathrm{NM}}\,d\mathcal{B}), \\
\langle x, h_5\rangle &= \alpha_4\left[1-\frac{1}{2}F\left(d\psi_{\mathrm{NM}}^2\right) - \frac{1}{2}F\left(d\mathcal{B}^2\right)\right] + \alpha_3 F(d\psi_{\mathrm{NM}}) \\
&\quad +\alpha_6 F(d\mathcal{B}) + \alpha_5 F(d\psi_{\mathrm{NM}}\,d\mathcal{B}), \\
\langle x, h_3\rangle &= \alpha_5\left[1-\frac{1}{2}F\left(d\psi_{\mathrm{NM}}^2\right) - \frac{1}{2}F\left(d\mathcal{B}^2\right)\right] - \alpha_6 F(d\psi_{\mathrm{NM}}) \\
&\quad -\alpha_3 F(d\mathcal{B}) + \alpha_4 F(d\psi_{\mathrm{NM}}\,d\mathcal{B}), \\
\langle x, h_6\rangle &= \alpha_6\left[1-\frac{1}{2}F\left(d\psi_{\mathrm{NM}}^2\right) - \frac{1}{2}F\left(d\mathcal{B}^2\right)\right] + \alpha_5 F(d\psi_{\mathrm{NM}}) \\
&\quad -\alpha_4 F(d\mathcal{B}) - \alpha_3 F(d\psi_{\mathrm{NM}}\,d\mathcal{B}), \quad (18)
\end{aligned}$$

where F is a functional (originally defined in Ref. [42] as $\mathcal{J}$) given by

$$F(a) = \frac{1}{I_7}\int_{f_{\min}/f_0}^{f_{\max}/f_0} dx\,\frac{x^{-7/3}}{S_h(xf_0)}a(x) \qquad (19)$$

and the noise moment I is itself defined as

$$I_q \equiv \int_{f_{\min}/f_0}^{f_{\max}/f_0} dx\,\frac{x^{-q/3}}{S_h(xf_0)} \qquad (20)$$

where $f_{\min}$ and $f_{\max}$ define the range of frequencies we integrate over. In S3 we used a lower cutoff frequency of 70 Hz, chosen to exclude lower frequencies for which the detector's power spectral density was significantly non-stationary, and an upper frequency corresponding to the Nyquist frequency,

in this case 1024 Hz. Inserting the relations from Eq. (18) into Eq. (11) and keeping up to second order perturbations, we obtain

$$\sum_{j=1}^{6} \langle x, h_j \rangle^2 = \sum_{j=1}^{6} \alpha_j^2 \left[1 - F(d\psi_{\mathrm{NM}}^2) + F(d\psi_{\mathrm{NM}})^2 \right]$$
$$- \sum_{j=3}^{6} \alpha_j^2 \left[F(d\mathcal{B}^2) - F(d\mathcal{B})^2 \right]$$
$$- \left[2 \left(\alpha_3 \alpha_6 - \alpha_4 \alpha_5 \right) \right.$$
$$\left. \times \left[F(d\psi_{\mathrm{NM}} \, d\mathcal{B}) - F(d\psi_{\mathrm{NM}})F(d\mathcal{B}) \right] \right] . (21)$$

To finish computing the perturbed ρ^2 we must maximize Eq. (21) over the coalescence time and α_j (subject to the constraint $\sum_{j=1}^{6} \alpha_j^2 = 1$ since we are dealing with normalized waveforms). Maximization over α_j is performed straightforwardly using Lagrange multipliers. We find $\alpha_1 = \alpha_2 = 0$, $\alpha_3 = -\alpha_6$, and $\alpha_4 = \alpha_5$, which leads to

$$\max_{\alpha_j} \quad \langle x, h_j \rangle^2 = 1 - F(d\psi_{\mathrm{NM}}^2) + F(d\psi_{\mathrm{NM}})^2 - F(d\mathcal{B}^2)$$
$$+ F(d\mathcal{B})^2 + F(d\psi_{\mathrm{NM}} \, d\mathcal{B}) - F(d\psi_{\mathrm{NM}})F(d\mathcal{B}). \quad (22)$$

We incorporate the time-dependence of ρ^2 into the template's phasing and expand the phase functions in terms of the phenomenological parameters and coalescence time t_c

$$d\psi_{\mathrm{NM}} = d\psi_0 \, f^{-5/3} + d\psi_3 \, f^{-2/3} + 2\pi f dt_c, \quad (23)$$
$$d\mathcal{B} = d\beta \, f^{-2/3}. \quad (24)$$

Using the definition of the metric [42] to write

$$\rho^2 = 1 - 2g_{ab}d\lambda^a d\lambda^b, \quad (25)$$

we obtain the metric components

$$2g_{t_c t_c} = 4\pi^2 \left(J_1 - J_4^2 \right),$$
$$2g_{t_c \psi_0} = 2\pi \left(J_9 - J_4 J_{12} \right),$$
$$2g_{t_c \psi_3} = 2\pi \left(J_6 - J_4 J_9 \right),$$
$$2g_{t_c \beta} = (-\pi/2) \left(J_6 - J_4 J_9 \right),$$
$$2g_{\psi_0 \psi_0} = J_{17} - J_{12}^2,$$
$$2g_{\psi_0 \psi_3} = J_{14} - J_9 J_{12},$$
$$2g_{\psi_0 \beta} = (-1/2) \left(J_{14} - J_9 J_{12} \right),$$
$$2g_{\psi_3 \psi_3} = J_{11} - J_9^2,$$
$$2g_{\psi_3 \beta} = (-1/2) \left(J_{11} - J_9^2 \right),$$
$$2g_{\beta \beta} = J_{11} - J_9^2 \quad (26)$$

before projecting out the coalescence time t_c. Here we have used J_q to represent the normalized noise moments given by [48]

$$J_q \equiv I_q / I_7 \quad (27)$$

where the noise moment I was defined in Eq. (20). These moments give us a way of checking when the strong modulation approximation is valid.
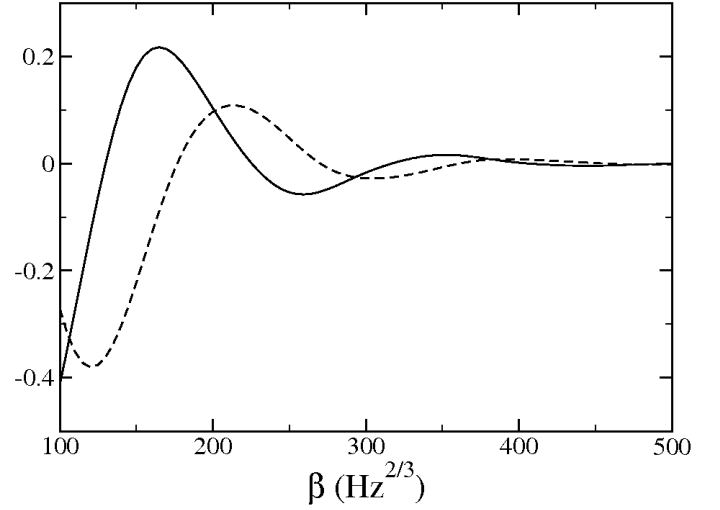

FIG. 2: Moment functions $C_7(\beta)$ (solid line) and $S_7(\beta)$ (dashed line) for the initial LIGO design noise power spectral density. For values of $\beta \gtrsim 200$ Hz$^{2/3}$ we see that these moments become small and can be neglected - this is what we call the *strong modulation approximation*.

If we had not made the strong modulation approximation, we would also need the functions

$$C_p(\beta) = \int_0^\infty df \left[f^{p/3} S_h(f) \right]^{-1} \cos \mathcal{B}(f)/I_7, \quad (28)$$
$$S_p(\beta) = \int_0^\infty df \left[f^{p/3} S_h(f) \right]^{-1} \sin \mathcal{B}(f)/I_7, \quad (29)$$

which we call the cosine and sine moment functions. The inner products of the basis templates h_j with each other (prior to the Gram-Schmidt procedure) are proportional to these moment functions, and thus the strong modulation approximation corresponds to assuming that C_7 and S_7 are small compared to unity. For the initial LIGO design noise power spectral density curve [49] the moment functions are plotted in Fig. 2. We see that the strong modulation approximation should hold (to about the 10% level) for $\beta \gtrsim 200$ Hz$^{2/3}$. See also Fig. 15 of Ref. [41], discussed more below, which shows approximately the same behavior.

After projecting the coalescence time out of Eq. (26) and dropping $\psi\beta$ cross terms (which simplifies the template placement and changes the volume per template by less than 3%), we obtain

$$2g_{\psi_0 \psi_0} = J_{17} - J_{12}^2 - \left(J_9 - J_4 J_{12} \right)^2 / \left(J_1 - J_4^2 \right),$$
$$2g_{\psi_0 \psi_3} = J_{14} - J_9 J_{12} - (J_6 - J_4 J_9)(J_9 - J_4 J_{12})$$
$$/ \left(J_1 - J_4^2 \right),$$
$$2g_{\psi_0 \beta} = 0,$$
$$2g_{\psi_3 \psi_3} = J_{11} - J_9^2 - (J_6 - J_4 J_9)^2 / \left(J_1 - J_4^2 \right),$$
$$2g_{\psi_3 \beta} = 0,$$
$$2g_{\beta \beta} = J_{11} - J_9^2 - (J_6 - J_4 J_9)^2 / 4 \left(J_1 - J_4^2 \right). \quad (30)$$

B. Template placement algorithm

We set the density of our template bank in terms of the *minimal match* (MM), defined to be the lowest match that can be obtained between a signal and the nearest template [42]. A template bank designed to have minimal match $MM = 0.95$ would therefore suffer no more than a $1 - MM = 5\%$ loss in SNR due to mismatch between the parameters of a signal and the best possible template in the bank (assuming that the signal and templates are from the same family).

The metric components shown in Eq. (30) are constant in the strong modulation approximation, which enables us to use a simple template placement algorithm. We use a body-centred cubic (BCC) lattice which is the most efficient template placement in three dimensions. We first diagonalize the metric, which leaves the β parameter unchanged but gives us new "horizontal" parameters ψ_0' and ψ_3'. Starting on the plane $\beta = 0$, we draw a box in the primed coordinates which encloses the part of that plane to be searched. Beginning at one corner of this box, we step in the primed "horizontal" coordinates by amounts $(4/3)\sqrt{2(1 - MM)/E}$, where E is the corresponding eigenvalue of the metric, i.e., $g_{\psi_0'\psi_0'}$ or $g_{\psi_3'\psi_3'}$. At each point we transform to the mass parameters using Eqs. (13) and (14) and check if we are in the targeted region of physical mass space. If the point is within that region, we add a template to the list. Once a plane of constant β is filled, we move "up" a distance in β equal to $(2/3)\sqrt{2(1 - MM)/g_{\beta\beta}}$, and lay a "horizontal" grid which is staggered half a cell (in both primed directions) from the previous one. Thus a BCC lattice is formed.

Such a simple template placement algorithm is susceptible to the "ragged edges" problem. That is, there will be some areas near the edge of the targeted region of parameter space that will match the nearest template at a level less than MM. The problem appears in other template placement algorithms such as those of Refs. [25, 43], and sometimes is addressed in a complicated way. Our solution is simple and practical. In stepping around the (ψ_0', ψ_3') plane, we check to see if we have crossed the edge of the targeted region. If we find ourselves at a point outside of the targeted region, we check to see whether the point halfway between the current position and the previously laid template is itself within the targeted region. If so, we add a template there. Although the edges of the targeted region are curved, the radius of curvature is many template spacings meaning that we can treat the edges as fairly straight. This simple method solves the ragged edges problem while resulting in a small number of additional templates.

As mentioned earlier, we choose f_{cut}, the frequency at which we end our template, to be the frequency of gravitational wave emission at the last stable orbit. However, we compute metric components by effectively taking f_{cut} to infinity, which gains us simplicity at the cost of a small over-coverage.

We can compare the simplified template bank used here to those proposed in the literature, particularly in Refs. [41, 44]. Although neither of those articles actually constructs a template bank or gives explicit metric components, we can find a point of comparison. Figure 15 of Ref. [41] plots the coordi-

nate volume per template as a function of β, assuming a simple cubic lattice with $MM = 0.97$ and an analytical approximation to the initial LIGO noise curve. In the high-β (strong modulation) limit, their volume tends to $\sim 5 \times 10^6$ Hz^3. For the same MM, lattice, and noise curve, our volume per template is $\sim 6.4 \times 10^6$ Hz^3. Thus, our grid is slightly sparser than that of Ref. [41]. Most of the difference is because they define their final metric (on the space of intrinsic parameters only) in terms of a "minimax" overlap, which is more restrictive than the metric described here. The issue is that the spacing on the intrinsic parameter space in general depends on the extrinsic parameters, and there are multiple ways to remove this dependence. The minimax criterion of Ref. [41] assumes the worst case (in terms of extrinsic parameters) or tightest spacing for each point in parameter space, and thus is tighter (lower template volume) than it needs to be. Spin-induced precession of the orbital plane will cause sidebands either side of the carrier frequency. The metric we describe is constructed implicitly assuming that there is always non-zero power at the carrier frequency and both precession sidebands, which eliminates a set of measure zero of worst-case points in the extrinsic parameter space. The template bank tests described below verify that the loss of efficiency due to neglecting the worst-case extrinsic parameters is no more than a few percent.

For the real S3 noise spectra which were used to construct the template banks in this search, template numbers were typically $2 - 6 \times 10^3$ in H1 and L1 when prescribing a minimal match of 0.95. The number of templates was larger in H2 compared to the other detectors and also increased with time to $\sim 1.6 \times 10^4$ towards the end of S3 due to a flattening of the noise power spectrum in H2. Although a minimal match of 0.95 was prescribed the effective minimal match of the template banks generated was reduced to ~ 0.93 due to a small calculation error. Figure 3 shows a template bank generated using 2048 seconds of H1 data and with a prescribed minimal match of 0.95.

C. Testing the template bank

The template bank was tested using a series of simulated signals constructed using the equations of the target waveforms described in Sec. III. We considered a variety of spin configurations including systems where neither, one or both bodies were spinning. We also considered masses outside the range we expected the template bank to have good coverage in order to fully evaluate the range of masses for which it could be used. For each spin configuration we created a series of signals corresponding to every mass combination: $1.0 \, M_\odot < m_1, m_2 < 20.0 \, M_\odot$. Using the initial LIGO design sensitivity we then measured the best match that could be obtained for every signal using our template bank. Figure 4 shows a sample of the results from the tests of the template bank. As expected we found that our template bank achieved the highest matches for non-spinning (and therefore non-precessing) binaries. Performance degrades as spin-precessional effects become more pronounced i.e., when both bodies are spinning maximally with spins misaligned from
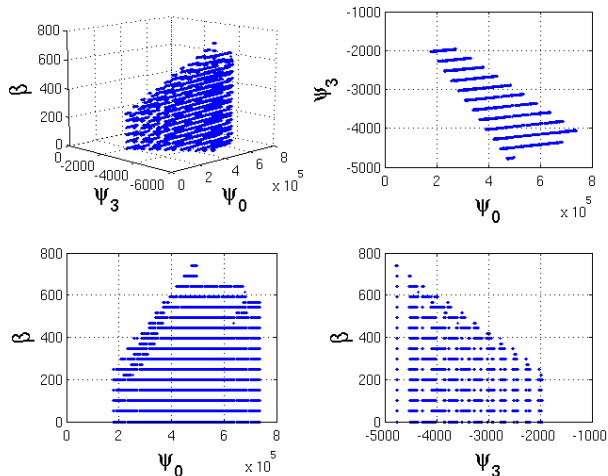
FIG. 3: A template bank generated with minimal match $= 0.95$ using 2048 seconds of H1 data taken during S3. The crosses show the positions of individual templates in the (ψ_0, ψ_3, β) parameter space. For each template a value for the cutoff frequency f_{cut} is estimated using Eq. 8. This bank requires a 3-dimensional template placement scheme in order to place templates in the (ψ_0, ψ_3, β) parameter space. Previous searches for non-spinning systems have used 2-dimensional placement schemes.
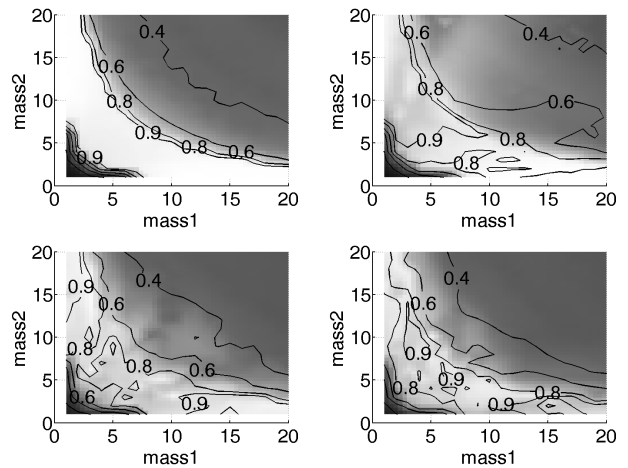

FIG. 4: Plots showing the best match achieved by filtering a series of simulated signals through the template bank described in this section. The values on the x and y axes correspond to the component masses of the binary source to which the simulated signal corresponds. The shade of grey in the plots shows the best match achieved for a given simulated signal. The four subplots correspond to four different spin-configurations of the binary source. The top-left subplot shows results for a non-spinning binary system. The top-right subplot shows results for a system consisting of one non-spinning object and one maximally spinning object with its spin slightly misaligned with the orbital angular momentum. We would expect this system to precess. The bottow two subplots show results for two generic precessing systems consisting of two maximally spinning bodies with spins and orbital angular momentum all misaligned from each other. We see that the region of the mass plane for which we obtain matches > 0.9 is largest for the non-spinning system and tends to be concentrated in the asymmetric mass region loosely bounded by $1.0\ M_\odot < m_1 < 3.0\ M_\odot$ and $12.0\ M_\odot < m_2 < 20.0\ M_\odot$.

the orbital angular momenta. The template achieved matches > 0.9 for a mass range $1.0\ M_\odot < m_1 < 3.0\ M_\odot$ and $12.0\ M_\odot < m_2 < 20.0\ M_\odot$ (and equivalent systems with m_1 and m_2 swapped). The detection template family (described in Sec. IV) is capable of obtaining high matches for comparable mass systems, the lower matches obtained for comparable mass systems are a result of targeting our template bank on asymmetric mass ratio systems (which are more susceptible to spin effects and conform to the strong modulation approximation).

Matches below the specified minimal match of 0.95 in the bank's region of good coverage are a consequence of (small) differences between the DTF and the target waveforms meaning that the DTF *cannot* perfectly match the target waveforms. The *fitting factor* (FF) measures the reduction of SNR due to differences between the DTF and the target waveform [17] (and should not be confused with the minimal match which measures the loss of SNR due to discreteness of the template bank [42]). The DTF performance is evaluated and its fitting factor is measured in Sec. VI of Ref. [19], for NS-BH systems an average FF of ≈ 0.93 was measured [62].

VI. SEARCH PIPELINE

The pipeline used for this search is the same as used in the other S3 searches for binary inspirals [7] and is described fully in a set of companion papers [26, 50]. This pipeline has been significantly updated since the S2 analysis and a brief summary is now given.

In Sec. VI A we discuss the S3 data set. In Sec. VI B we describe how we decide whether triggers measured in different detectors could be associated with the same gravitational wave event. In Sec. VI C we introduce the statistic which we use to assign SNRs to the events found in coincidence between two or more detectors. In Sec. VI D we describe how we estimate the expected rate of accidental coincidences.

A. Data sample

To begin with we construct a list of times for which two or more of the detectors are operating nominally, in what is referred to as *science mode*. By demanding that a gravitational wave be detected in coincidence between two or more detectors we simultaneously decrease the probability of inferring a detection when no true signal was present (a false alarm) and improve the confidence we have in a detection of a true signal. Data collected by the LHO detectors was only analyzed when both detectors were in science mode. This was due to concerns that since both of these detectors share the same vacuum system, the laser beam of a detector in anything

but science mode might interfere with the other detector.

We denote periods of time when all three detectors are in science mode as H1-H2-L1 times and periods when only the Hanford detectors are on as H1-H2 times. A coincident trigger consisting of a trigger in the H1 detector and the L1 detector will be referred to as an H1-L1 coincident trigger and similarly for other combinations of detectors.

In this search we analyze 184 hours of H1-H2-L1 data and 604 hours of H1-H2 data (see Table I). During these times we construct template banks for each detector and subsequently produce a list of triggers whose SNR exceeded our threshold.

Around 9% of the data is specified as *playground data* and is used to tune the various parameters (e.g., SNR thresholds and coincidence windows) used in the full search. Playground data is not included in the upper limit calculation but is still searched for possible detections. We also construct lists of *veto times* during which the data we analyze had poor data quality due to short stretches of instrumental or environmental noise [50, 51]. All coincident data is analyzed but gravitational wave candidates found during veto times will be subjected to greater scrutiny than those found during other times.

TABLE I: Summary of the amount of data analyzed in our various data sets. In S3 we only analyze data from the LHO detectors when both H1 and H2 are in science mode. Around 9% of the data is classified as *playground data* and is used to tune the parameters of the search.

Data type	Total analyzed (hours)	Non-playground (hours)
H1-H2	604	548
H1-H2-L1	184	167

We can compare the sensitivities of the LIGO detectors by measuring the *horizon distance* of a particular source — this is the distance to which an optimally oriented source can be observed with SNR = 8. In Fig. 5 we plot the horizon distance of a $(2, 16)M_\odot$ binary. This choice of component mass reflects that the template bank used for this search (see Section V) achieves highest matches for asymmetric binaries. In Fig. 1 of [7] the horizon distance for a range of symmetric binaries is shown.

B. Coincident analysis

To minimize the false alarm probability we demand that a gravitational wave signal be observed by two or more detectors with similar parameters. In order to determine whether a trigger measured by one particular detector should be considered as coincident with a trigger in another detector we define a set of coincidence windows. In this search we demand that for triggers from different detectors to be considered as coincident they must satisfy the following conditions:

$$|t_1 - t_2| < \Delta t_1 + \Delta t_2 + T_{1,2}, \quad (31)$$
$$|\psi_{0,1} - \psi_{0,2}| < \Delta \psi_{0,1} + \Delta \psi_{0,2} \quad (32)$$
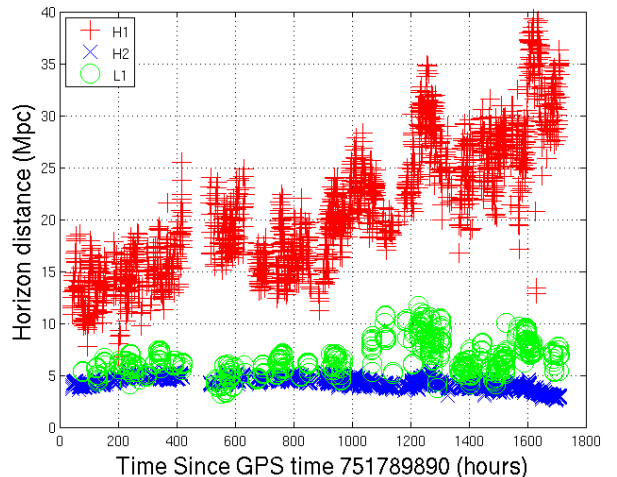$$|\psi_{3,1} - \psi_{3,2}| < \Delta \psi_{3,1} + \Delta \psi_{3,2} \quad (33)$$

FIG. 5: Distance to which an optimally oriented non-spinning $(2, 16)M_\odot$ binary can be detected with SNR = 8 throughout S3. For systems with spinning components, the horizon distance would be equal or less than what is shown in this figure since any spin-induced precession would cause the system to become less than optimally oriented and therefore reduce the measured amplitude of its emission. We see a large improvement in the sensitivity of H1 during this science run.

where t_i, $\psi_{0,i}$ and $\psi_{3,i}$ are the measured time of coalescence and phenomenological mass parameters measured using our template bank in detector i; Δt_i, $\Delta \psi_{0,i}$ and $\Delta \psi_{3,i}$ are our coincidence windows in detector i and $T_{i,j}$ is the light travel time between detector locations i and j. The light travel time between LHO and LLO is ~ 10 ms.

We tune our coincidence windows on the playground data in order to recover as many of our simulated signals as possible whilst trying to minimize the false alarm rate. The use of playground data allows us to tune our search parameters without biasing the results of our full analysis. The tuning method used for this and the non-spinning search on S3/S4 data is described fully in [50]. Using this tuning method we find our coincidence windows to be equal for each detector with values $\Delta t = 100$ ms, $\Delta \psi_0 = 40,000$ Hz$^{5/3}$ and $\Delta \psi_3 = 600$ Hz$^{2/3}$. The value of Δt used in this search is four times larger than the 25 ms value used in the S3 search for non-spinning binary black holes [7] indicating that the estimation of arrival time of a gravitational waveform is less well determined in this search than in the non-spinning search.

C. Combined SNR

For coincident triggers we use a combined signal-to-noise ratio ρ_c statistic based upon the individual signal-to-noise ratios ρ_i measured by each detector:

$$\rho_c^2 = \min \left\{ \sum_i \rho_i^2, (a\rho_i - b)^2 \right\}. \quad (34)$$

In practice the parameters a and b are tuned so that the contours of false alarm generated using Eq. (34) separate triggers generated by software injection of simulated signals and background triggers as cleanly as possible [50] (see the next subsection for details of how we estimate the background). In this search we used values $a = b = 3$ for all detectors. For coincident triggers found in all three detectors we use:

$$\rho_c^2 = \sum_i \rho_i^2. \tag{35}$$

D. Background Estimation

We estimate the rate of accidental coincidences, otherwise known as the background or false alarm rate, for this search through analysis of time-shifted data. We time-shift the triggers obtained from each detector relative to each other and then repeat our analysis, searching for triggers that occur in coincidence between 2 or more of the detectors. By choosing our time-shifts to be suitably large ($\gg 10$ ms light travel time between LHO and LLO) we ensure that none of the coincident triggers identified in our time-shift analysis could be caused by a true gravitational wave signal and can therefore be used as an estimate of the rate of accidental coincidences. In practice we leave H1 data unshifted and time-shift H2 and L1 by increments of 10 and 5 s respectively. In this search, we analyzed 100 sets of time-shifted data (50 forward shifts and 50 backward shifts). For clarity we will use the term *in-time* to mean triggers which have not been time-shifted.

VII. VETOES

A. Instrument based vetoes

We are able to veto some background triggers by observing correlation between the gravitational wave channel (AS_Q) of a particular detector and one or more of its auxiliary channels which monitor the local physical environment. Since we would not expect a true gravitational wave signal to excite the auxiliary channels, we will treat as suspicious any excitation in the gravitational wave channel that is coincident in time with excitations in the auxiliary channels. A list of auxiliary channels found to effectively veto spurious (non-gravitational wave coincident triggers) were identified and used for all S3 searches [51]. Additional vetoes based upon other auxiliary channels were considered but were subsequently abandoned because the total amount of data these channels would have discounted, known as the *dead-time*, was unacceptably large.

B. Signal based vetoes

We can use the fact that the Hanford detectors are co-located to veto coincident triggers whose measured amplitude is not consistent between H1 and H2. We check for consistency between the SNR values measured using H1 and H2 data for triggers found in coincidence. Since H1 is the more sensitive instrument we simply required that the SNR measured in H1 be greater than that measured in H2 for an event to survive this veto. Since data from H1 and H2 was only analysed when both were in science mode, this veto means that there will be no H2-L1 coincident triggers since this would indicate that H2 had detected a trigger which H1 was unable to detect.

The χ^2 veto used for the primordial black hole and binary neutron star searches [7] has not not been investigated for use in searches using detection template families (i.e., this search and the S2-S4 searches for non-spinning binary black holes [7, 13]).

VIII. RESULTS

In the search of the S3 LIGO data described in this paper, no triple-coincident event candidates (exceeding our predetermined SNR threshold and satisfying the coincidence requirements described in Sec. VI B) were found in triple-time (H1-H2-L1) data. Many double-coincident event candidates were found in both triple-time and double-time (H1-H2) data.

A cumulative histogram of combined SNR for in-time and background coincident triggers is shown in Fig. 6. We see that, at the SNR threshold (i.e., the leftmost points on this figure), the number of in-time double-coincident triggers is consistent with the number of coincident triggers yielded by the time-shift analysis. The small excess in the number of in-time H1-H2 coincident triggers at higher SNRs indicates that there is some correlation between the LHO detectors. The coincident triggers contributing to this excess have been investigated and are not believed to be caused by gravitational waves. Seismic activity at the Hanford site has been recorded throughout S3 and can cause data to become noisy simultaneously in H1 and H2. Coincident triggers caused by seismic noise will predominantly cause only in-time coincidences (although time-shift coincidences caused by two seismic events separated in time but shifted together can occur) leading to an excess of in-time coincident triggers as we have observed in Fig. 6. As mentioned previously, there were no coincident triggers observed by all three detectors.

A scatter plot of the SNRs measured for coincident triggers in H1-H2 times is shown in Fig. 7. The distribution of our in-time triggers is consistent with our estimation of the background. This is also true for the double-coincident triggers measured in H1-H2-L1 times.

The loudest in-time coincident trigger was observed in H1-H2 when only the Hanford detectors were in science mode. This event candidate is measured to have SNRs of 119.3 in H1, 20.4 in H2 and a combined SNR of 58.3. The loudest coincident triggers are subjected to systematic follow-up investigations in which a variety of information (e.g., data quality at time of triggers, correlation between the detector's auxiliary channels and the gravitational wave channel) is used to assess whether the coincident triggers could be confidently claimed as detection of gravitational wave events. This event is found at a time flagged for "conditional" vetoing. This

means that during these times some of the detectors auxiliary channels exhibited correlation with the gravitational wave channel (AS_Q) and that we should be careful in how we treat event candidates found in these times. For this particular coincident trigger an auxiliary channel indicated an increased numbers of dust particles passing through the dark port beam of the interferometer [51]. Upon further investigation it was found that this coincident trigger occurred during a period of seismic activity at the Hanford site and we subsequently discounted this candidate as a potential gravitational wave event. Time-frequency images of the gravitational wave channel around the time of this candidate were inconsistent with expectations of what an inspiral signal should look like, further reducing the plausibility of this candidate being a true gravitational wave event. It is interesting, but unsurprising, to note that during the search for non-spinning binary black holes that also used S3 LIGO data, high-SNR triggers associated with this seismic activity were also detected [7]. Furthermore, the 20 next loudest event candidates were also investigated and none were found to be plausible gravitational wave event candidates. Work is in progress to automate the follow-up investigative procedure and to include new techniques including null-stream and Markov chain Monte Carlo analysis for assessing the plausibility of coincident triggers as gravitational wave events.
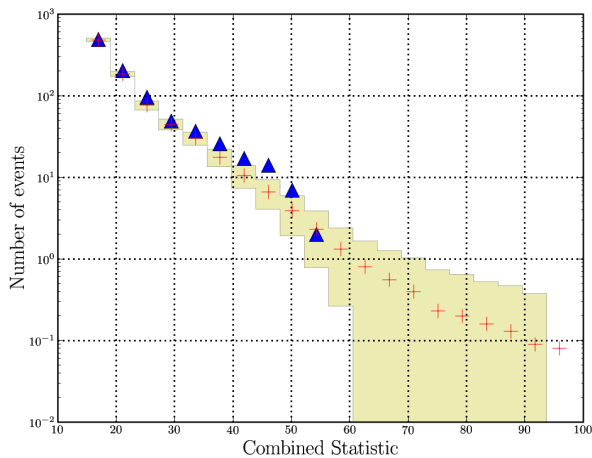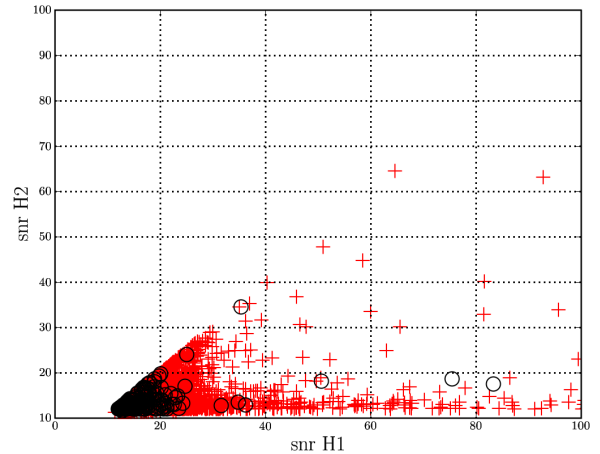

FIG. 7: Scatter plot of SNR for coincident triggers in H1-H2 times. The black circles represent in-time coincident triggers and the light colored (red) pluses represent time-shift coincident triggers that we use to estimate the background. Note that due to our signal based veto on H1/H2 SNR we see no coincident triggers with $\rho_{H1} < \rho_{H2}$.
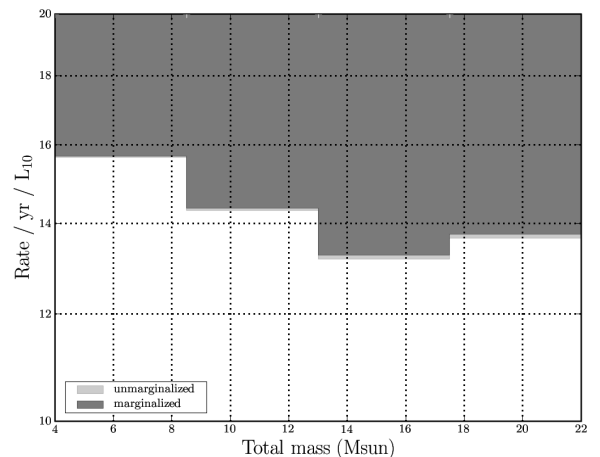

FIG. 6: Cumulative histograms of the combined SNR, ρ_c for in-time coincident triggers (triangles) and our background (crosses with one-sigma deviation shown) for all H1-H2 and H1-H2-L1 times within S3. We see a small excess in the number of in-time coincident triggers with combined SNR ~ 45. This excess was investigated and was caused by an excess of H1-H2 coincident triggers. Since H1 and H2 are co-located, both detectors are affected by the same local disturbances (e.g., seismic activity) which contributes to the number of in-time coincidences but which is under-represented in time-shift estimates of the background.

FIG. 8: Upper limits on the spinning binary coalescence rate per L_{10} as a function of the total mass of the binary. For this calculation, we have evaluated the efficiency of the search using a population of binary systems with $m_1 = 1.35M_\odot$ and m_2 uniformly distributed between 2 and $20M_\odot$. The darker area on the plot shows the region excluded after marginalization over the estimated systematic errors whereas the lighter region shows the region excluded if these systematic errors are ignored. The effect of marginalization is typically small ($< 1\%$). The initial decrease in the upper limit corresponds to the increasing amplitude of the signals as total mass increases. The subsequent increase in upper limit is due to the counter effect that as total mass increases the signals become shorter and have fewer cycles in LIGO's frequency band of good sensitivity.

IX. UPPER LIMITS

Given the absence of plausible detection candidates within the search described above, we have calculated an upper limit on the rate of spinning compact object coalescence in the universe. We quote the upper limit rate in units of $\mathrm{yr}^{-1}\mathrm{L}_{10}^{-1}$ where $\mathrm{L}_{10} = 10^{10}\,\mathrm{L}_{\odot,\mathrm{B}}$ is 10^{10} times the blue light luminosity of the sun.

The absorption-corrected blue light luminosity of a galaxy infers its massive star formation rate which we assume scales with the rate of compact binary coalescence within it [52]. This assumption is well justified when the galaxies reached by the detector are dominated by spiral galaxies with ongoing star formation (e.g., the Milky Way). Results papers reporting on S1 and S2 [13, 53, 54] have quoted the upper limit in units of Milky Way Equivalent Galaxy (MWEG) which is equivalent to about $1.7\,\mathrm{L}_{10}$. Upper limits on the rate of coalescences calculated during other searches using S3 and S4 LIGO are given in units of L_{10} [7].

The upper limit calculations are based on the loudest event statistic [55, 56], which uses both the detection efficiency at the combined SNR of the loudest event candidate and the associated background probability. The in-time non-playground data set (which we use to set the upper limit) is *blinded* in the sense that all analysis parameters are tuned (as described in Secs. VI) prior to its analysis.

The Bayesian upper limit at a confidence level α, assuming a uniform prior on the rate R, is given by [56]

$$1 - \alpha = e^{-R T \mathcal{C}_L(\rho_{c,\max})} \left[1 + \left(\frac{\Lambda}{1+\Lambda} \right) R T \mathcal{C}_L(\rho_{c,\max}) \right] \tag{36}$$

where $\mathcal{C}_L(\rho_{c,\max})$ is the cumulative blue light luminosity to which we are sensitive at a given value of combined SNR $\rho_{c,\max}$, T is the observation time, and Λ is a measure of the likelihood that the loudest event is consistent with being a signal and inconsistent with background (as estimated using time-shifts). We evaluate the cumulative luminosity $\mathcal{C}_L$ at the combined SNR of the loudest coincident trigger seen in this search, $\rho_{c,\max} = 58.3$ (see Sec. VIII for discussion of this coincident trigger). The expression for Λ is

$$\Lambda = \frac{|\mathcal{C}'_L(\rho_{c,\max})|}{P'_B(\rho_{c,\max})} \left[\frac{\mathcal{C}_L(\rho_{c,\max})}{P_B(\rho_{c,\max})} \right]^{-1}, \tag{37}$$

where the derivatives are with respect to ρ_c. $P_B(\rho)$ is the probability that all background coincident triggers (as estimated using time-shifts) have a combined SNR less than ρ. For the loudest event candidate in this search we find $P_B = 0.23$ and $\Lambda = 0.05$. In the case where the loudest event candidate is most likely due to the background $\Lambda \to 0$ and the upper limit becomes

$$R_{90\%} = \frac{2.3}{T \mathcal{C}_L(\rho_{c,\max})}. \tag{38}$$

In the limit of zero background, i.e., the event is definitely not background, $\Lambda \to \infty$ and the numerator in Eq. (38) becomes 3.9. The observation time T is taken from Table I, where we use the analyzed time *not* in the playground. This is consistent with our blind analysis strategy.

In searches for systems consisting of non-spinning bodies efficiency is typically found as a function of its effective distance and chirp mass [57]. For a system consisting of non-spinning bodies effective distance can be calculated using the distance to the source, its inclination with respect to the detector and the detector's antenna response functions (see Eq. (2) of [7] and [5]). For a system consisting of spinning bodies, its inclination with respect to a detector will evolve during the course of the inspiral making the calculation of effective distance complicated. Instead, in this search we find efficiency and predicted source luminosity as a function of the inverse of the *expected SNR* of a source. The expected SNR is defined as the SNR that would be obtained for a given simulated source assuming we use a template that perfectly matches the emitted gravitational waveform and a detector whose noise power spectrum we can estimate accurately. By taking the inverse of the expected SNR we obtain a quantity which behaves similarly to the effective distance by taking larger values for signals which are nearer and/or optimally oriented to the detector and thus more easily detectable and by taking smaller values as the signals become less detectable.

Following the tests of the template bank (Sec. V C) we also know that the efficiency at which we are able to detect sources will depend on their spins as well as their effective distance and component masses. In this upper limit calculation we assess the efficiency of the search using software injection of simulated signals representing a population of sources with spins randomized so that i) the spin magnitude of each of the compact objects is distributed uniformly in the range $0 < \chi < 1$ and ii) the direction of compact object's spin is uniformly distributed on the surface of a sphere. The distances of the simulated sources are chosen uniformly on a logarithmic scale. The sky-positions and initial polarization and inclination angles of the simulated sources are all chosen randomly and to be uniformly distributed on the surface of a sphere. We evaluated the efficiency of this search for masses in the range $1.0\,M_\odot < m_1, m_2 < 20.0\,M_\odot$. During S3, LIGO's efficiency was dominated by sources within the Milky Way for which detection efficiency was high across the entire mass range investigated due to the proximity of these sources to Earth. We also had some detection efficiency for binaries in M31 and M33.

The cumulative luminosity $\mathcal{C}_L(\rho_c)$ can be obtained by generating a population of simulated signals using information on the observed distribution of sources from standard astronomy catalogs. We use a model based on [58] for the distribution of blue light luminosity throughout the nearby Universe. We use software injection of simulated signals (the target waveforms described in Sec. III) to evaluate the efficiency $\mathcal{E}$ for observing an event with combined SNR greater than ρ_c, as a function of the source's expected SNR. We then integrate $\mathcal{E}$ times the predicted source luminosity L as a function of expected SNR and mass. Since a binary system will generally have slightly different orientations with respect to the two LIGO observatory sites, the detectors at the two sites will both measure slightly different expected SNRs. The source's luminosity and the effi-

ciency with which it is detected are functions of both expected

SNRs, and the integration needed is two-dimensional:

$$\mathcal{C}_L(\rho_c) = \int_0^\infty \int_0^\infty \mathcal{E}(D_{\rho,\mathrm{H}}, D_{\rho,\mathrm{L}}, \rho)\, L(D_{\rho,\mathrm{H}}, dD_{\rho,\mathrm{L}})\, dD_{\rho,\mathrm{L}}\, dD_{\rho,\mathrm{H}} \qquad (39)$$

where D_ρ is the distance measure equal to the inverse of the expected SNR, at LHO (H) or LLO (L). As mentioned earlier, we evaluate $\mathcal{C}_L$ at $\rho_{c,\max} = 58.3$. The cumulative luminosity was measured to be $\sim 1.9 L_{10}$ and is dominated by the Milky Way ($1.7 L_{10}$) with the remainder made up by M31 and M33.

We calculate the upper limit on the rate of coalescence for proto-typical NS-BH binaries with masses $m_1 \sim 1.35\ M_\odot$ and $m_2 \sim 5\ M_\odot$. These values correspond to a population of NS-BH binaries with component masses similar to those used to assess the NS-NS and BH-BH upper limits in [7]. To calculate this upper limit we evaluate the efficiency of our search using binaries with a Gaussian mass distribution with means, $m_1 = 1.35\ M_\odot$ and $m_2 = 5\ M_\odot$ with standard deviations $\sigma_1 = 0.04\ M_\odot$ and $\sigma_2 = 1\ M_\odot$. These efficiencies are measured with simulated injected signals, using the same pipeline we used to find our candidates, counting the number of injections detected with SNR above $\rho_{c,\max}$, and the number missed. Assuming a Gaussian distribution of masses, we obtain an upper limit of $\mathcal{R}_{90\%} = 15.8\,\mathrm{yr}^{-1}\,\mathrm{L_{10}}^{-1}$. The upper limit calculation takes into account the possible systematic uncertainties which arise in this search, which are described in some detail in [57], and we will follow the analysis presented there to calculate the systematic errors for the above result. The most significant effects are due to the possible calibration inaccuracies of the detectors (estimated using hardware injections of simulated signals) and the finite number of Monte Carlo injections performed.

We must also evaluate the systematic errors associated with the chosen astrophysical model of potential sources within the galaxy. We obtain upper limits on the rate after marginalization over the estimated systematic errors, as described in [56, 57]. After marginalization over these errors we obtain an upper limit of $\mathcal{R}_{90\%} = 15.9\,\mathrm{yr}^{-1}\,\mathrm{L_{10}}^{-1}$.

We also calculate upper limits for a range of binary systems with $m_1 = 1.35 M_\odot$ and m_2 uniformly distributed between 2 and $20 M_\odot$. These upper limits, both before and after marginalization are shown in Fig. 8.

X. CONCLUSIONS

In this paper we have described the first search for gravitational waves emitted during the inspiral of compact binaries with spinning component bodies, which was carried out using data taken during the third LIGO science run. Interaction between the binary's orbital angular momentum and the spin angular momenta of its components will cause precession of its orbital plane resulting in the modulation of the observed

gravitational wave.

This search uses a detection template family designed specially to capture the spin-induced modulations of the gravitational waveform which could have resulted in them being missed by other searches targeted at non-spinning systems. The search pipeline used to carry out this and the other recent inspiral searches has been significantly improved since S2 and is fully described in a companion paper [7].

There were no plausible gravitational wave event candidates detected within the 788 hours of S3 data analyzed. The upper limit on the rate of coalescence for prototypical NS-BH binaries with spinning component bodies was calculated to be $\mathcal{R}_{90\%} = 15.9\,\mathrm{yr}^{-1}\,\mathrm{L_{10}}^{-1}$ once errors had been marginalized over.

The S5 LIGO data is greatly improved in sensitivity and observation time than previous data sets. There is considerable work in progress to further improve the techniques used to search for binaries with spinning component bodies using the S5 data. This includes development of an improved parameter-space metric which does not depend on the strong modulation approximation and allows us to search a larger region of parameter space, including binaries with comparable masses. Preparation for another search for binaries with spinning component bodies using a template family described by physical (rather than phenomenological) parameters [44] is also underway.

P070102-06-Z.

[1] B. Abbott et al. (LIGO Scientific Collaboration), Nucl. Instrum. Methods **A517**, 154 (2004).

[2] B. C. Barish and R. Weiss, Phys. Today **52 (Oct)**, 44 (1999).

[3] H. Lück and the GEO600 team, Class. Quant. Grav. **14**, 1471 (1997), *ibid*, **23**, S71 (2006).

[4] F. Acernese, P. Amico, M. Alshourbagy, F. Antonucci, S. Aoudia, S. Avino, D. Babusci, G. Ballardin, F. Barone, L. Barsotti, et al., Classical and Quantum Gravity **23**, S635 (2006), URL http://stacks.iop.org/0264-9381/23/S635.

[5] K. S. Thorne, in *Three hundred years of gravitation*, edited by S. W. Hawking and W. Israel (Cambridge University Press, Cambridge, 1987), chap. 9, pp. 330–458.

[6] L. P. Grishchuk, V. M. Lipunov, K. A. Postnov, M. E. Prokhorov, and B. S. Sathyaprakash, USP.FIZ.NAUK **171**, 3 (2001), URL http://arxiv.org/abs/astro-ph/0008481.

[7] B. Abbott et al. (LIGO Scientific Collaboration), gr-qc (2007), arXiv:0704.3368, to be submitted to Phys. Rev. D.

[8] S. F. Portegies Zwart and S. L. W. McMillan, Astrophys. J. **528**, L17 (2000).

[9] R. M. O'Leary, F. A. Rasio, J. M. Fregeau, N. Ivanova, and R. O'Shaughnessy, Astrophysical Journal **637**, 937 (2006), astro-ph/0508224. See also Kim et al., arXiv:0608280, and Kalogera et al., arXiv:0612144.

[10] J. M. Fregeau, S. L. Larson, M. C. Miller, R. O'Shaughnessy, and F. A. Rasio, Astrophysical Journal Letters **646**, L135 (2006), astro-ph/0605732.

[11] R. O'Shaughnessy, C. Kim, T. Fragos, V. Kalogera, and K. Belczynski, Astrophys. J. **633**, 1076 (2005), arXiv:astro-ph/0504479.

[12] R. O'Shaughnessy, C. Kim, V. Kalogera, and K. Belczynski (2006), astro-ph/0610076.

[13] B. Abbott et al. (LIGO Scientific Collaboration), Phys. Rev. D **73**, 062001 (2006), gr-qc/0509129.

[14] C. W. Helmstrom, *Statistical Theory of Signal Detection, 2nd edition* (Pergamon Press, London, 1968).

[15] T. A. Apostolatos, C. Cutler, G. J. Sussman, and K. S. Thorne, Phys. Rev. D **49**, 6274 (1994).

[16] L. E. Kidder, Physical Review D (Particles, Fields, Gravitation, and Cosmology) **52**, 821 (1995), URL http://link.aps.org/abstract/PRD/v52/p821.

[17] T. A. Apostolatos, Phys. Rev. D **52**, 605 (1995).

[18] T. A. Apostolatos, Phys. Rev. D **54**, 2438 (1996).

[19] A. Buonanno, Y. Chen, and M. Vallisneri, Phys. Rev. D **67**, 104025 (2003), erratum-ibid. 74 (2006) 029904(E).

[20] P. Grandclément, V. Kalogera, and A. Vecchio, Phys. Rev. D **67**, 042003 (2003).

[21] B. M. Barker and R. F. O'Connell, Phys. Rev. D **12**, 329 (1975).

[22] K. Belczynski, V. Kalogera, and T. Bulik, Astrophys. J. **572**, 407 (2002).

[23] V. Kalogera, Astrophys. J. **541**, 042003 (2000).

[24] R. O'Shaughnessy, J. Kaplan, V. Kalogera, and K. Belczynski, Astrophysical Journal **632**, 1035 (2005), astro-ph/0503219.

[25] S. Babak, Balasubramanian, D. Churches, T. Cokelaer, and B. Sathyaprakash, Class. Quant. Grav. **23**, 5477 (2006), gr-qc/0604037.

[26] B. A. Allen, W. G. Anderson, P. R. Brady, D. A. Brown, and J. D. E. Creighton (2005), gr-qc/0509116.

[27] P. Grandclément, M. Ihm, V. Kalogera, and K. Belczynski, Physical Review D (Particles, Fields, Gravitation, and Cosmology) **69**, 102002 (pages 10) (2004), URL http://link.aps.org/abstract/PRD/v69/e102002.

[28] K. S. Thorne, Astrophys. J. **191**, 507 (1974).

[29] G. B. Cook, S. L. Shapiro, and S. A. Teukolsky, Astrophys. J. **424**, 823 (1994).

[30] R. A. Remillard and J. E. McClintock, Annual Review of Astronomy and Astrophysics **44**, 49 (2006), URL http://www.citebase.org/abstract?id=oai:arXiv.org:astro-ph/0606352.

[31] J. E. McClintock, R. Shafee, R. Narayan, R. A. Remillard, S. W. Davis, and L.-X. Li, The Astrophysical Journal **652**, 518 (2006), URL http://www.citebase.org/abstract?id=oai:arXiv.org:astro-ph/0606076.

[32] T. Clifton and J. M. Weisberg, The Astrophysical Journal **679**, 687 (2008), http://www.journals.uchicago.edu/doi/pdf/10.1086/587049, URL http://www.journals.uchicago.edu/doi/abs/10.1086/587049.

[33] L. Blanchet, T. Damour, B. R. Iyer, C. M. Will, and A. G. Wiseman, Phys. Rev. Lett. **74**, 3515 (1995).

[34] L. Blanchet, B. R. Iyer, C. M. Will, and A. G. Wiseman, Class. Quant. Grav. **13**, 575 (1996).

[35] L. Blanchet, Phys. Rev. D **54**, 1417 (1996).

[36] L. Blanchet, G. Faye, B. R. Iyer, and B. Joguet, Phys. Rev. D **65**, 061501(R) (2002), gr-qc/0105099.

[37] L. E. Kidder, C. M. Will, and A. G. Wiseman, Phys. Rev. D **47**, R4183 (1993).

[38] T. Damour, B. R. Iyer, and B. S. Sathyaprakash, Phys. Rev. D **63**, 044023 (2001).

[39] L. Finn and D. Chernoff, Phys. Rev. D **47**, 2198 (1993).

[40] P. Grandclément and V. Kalogera, Phys. Rev. D **67**, 082002 (2003), gr-qc/0211075.

[41] A. Buonanno, Y. Chen, Y. Pan, H. Tagoshi, and M. Vallisneri, Phys. Rev. D **72**, 084027 (2005), gr-qc/0508064.

[42] B. J. Owen, Phys. Rev. D **53**, 6749 (1996).

[43] B. J. Owen and B. S. Sathyaprakash, Phys. Rev. D **60**, 022002 (1999).

[44] Y. Pan, A. Buonanno, Y.-b. Chen, and M. Vallisneri, Phys. Rev. D **69**, 104017 (2004), erratum-ibid. 74 (2006) 029905(E), gr-qc/0310034.

[45] A. Abramovici et al., Science **256**, 325 (1992).

[46] K. G. Arun, B. R. Iyer, B. S. Sathyaprakash, and P. A. Sundararajan, Physical Review D (Particles, Fields, Gravitation, and Cosmology) **71**, 084008 (pages 16) (2005), URL http://link.aps.org/abstract/PRD/v71/e084008.

[47] A. Buonanno, Y. Chen, and M. Vallisneri, Phys. Rev. D **67**, 024016 (2003), erratum-ibid. 74 (2006) 029903(E).

[48] E. Poisson and C. M. Will, Phys. Rev. **D52**, 848 (1995), gr-qc/9502040.

[49] A. Lazzarini and R. Weiss, Technical document LIGO-E950018-02-E (1996).

[50] The LIGO Scientific Collaboration, Tech. Rep. LIGO-T070109-01, LIGO Project (2007), URL http://www.ligo.caltech.edu/docs/T/T070109-01.pdf.

[51] N. Christensen et al. (LIGO Scientific Collaboration), Class.

Quant. Grav. **22**, S1059 (2005).

[52] E. S. Phinney, Astrophysical Journal **380**, L17 (1991).

[53] B. Abbott et al. (LIGO Scientific Collaboration), Phys. Rev. D **69**, 122001 (2004), gr-qc/0308069.

[54] B. Abbott et al. (LIGO Scientific Collaboration), Phys. Rev. D **72**, 082001 (2005), gr-qc/0505041.

[55] P. R. Brady, J. D. E. Creighton, and A. G. Wiseman, Class. Quant. Grav. **21**, S1775 (2004).

[56] R. Biswas, P. R. Brady, J. D. E. Creighton, and S. Fairhurst (2007), arXiv:0710.0465 [gr-qc].

[57] P. R. Brady and S. Fairhurst (2007), arXiv:0707.2410 [gr-qc].

[58] R. K. Kopparapu, C. R. Hanna, V. Kalogera, R. O'Shaughnessy, G. Gonzalez, P. R. Brady, and S. Fairhurst (2008), due to appear in ApJ March 2008, 676.

[59] W. H. Press, S. A. Teukolsky, W. T. Vetterling, and B. P. Flannery, *Numerical Recipes in C: The Art of Scientic Computing* (Cambridge University Press, Cambridge, England, 1992).

[60] The symbol ψ_3 used here is equivalent to the $\psi_{3/2}$ used in the papers by Buonanno, Chen and Vallisneri [19].

[61] Please note that a small error appears in Eq. (45) of [15]. The terms $1 + 3m_1/4m_2$ should in fact read $1 + 3m_2/4m_1$. Corrected forms of these expressions occur in Eq. (29) of [17]

[62] The authors of Ref. [19] use a downhill simplex method called AMOEBA[59] in order to obtain the best possible matches between the DTF and the target waveforms. This method works well for signals with high SNR but would not be effective in searching for weak signals in real detector data.